Solid Rocket Augmentation for Ram Accelerator Initial Launch

Clayton W. Davis

A thesis
submitted in partial fulfillment of the
requirements for the degree of

Master of Science

University of Washington

2019

Committee:

Carl Knowlen, Chair

Adam Bruckner

Program Authorized to Offer Degree:
Aeronautics and Astronautics

University of Washington

Abstract

Solid Rocket Augmentation for Ram Accelerator Initial Launch

Clayton W. Davis

Chair of the Supervisory Committee:
Carl Knowlen
Aeronautics and Astronautics

The ram accelerator is a hypervelocity launcher capable of speeds over 2 km/s and theoretically much higher. It operates by launching a projectile into a tube pre-filled with gaseous propellant, which combusts and generates thrust. The ram accelerator requires a minimum initial velocity which must be attained with a supplementary initial launcher. Single-stage light gas and conventional powder guns have traditionally been used for the initial launch. This study details the modeling and testing of an onboard solid rocket as an initial launcher for the ram accelerator. A quasi-one-dimensional model was developed and executed with a second-order MacCormack scheme with second- and fourth-order artificial diffusion terms. Atmospheric static fire and in-tube projectile cases were both considered theoretically and experimentally to evaluate the quasi-one-dimensional model. The accuracy of the model's inert gasdynamics were supported by experiment, but the combustion dynamics of the propellant were inaccurate. The rocket augmented projectile did not provide the velocity gains predicted by the quasi-one-dimensional model.

TABLE OF CONTENTS

LIST OF FIGURES

NOMENCLATURE

A	cross-sectional area
A_b	area of burning propellant
a	local sound speed
C	Courant number
c_p	specific heat at constant pressure
c_v	specific heat at constant volume
$\mathbf{D}$	total artificial viscosity vector
$\mathbf{d}$	combined artificial viscosity term
e	specific internal energy
$\mathbf{F}$	vector of flow variables
h_f	specific enthalpy of combustion products
i	cell spatial index
$\mathbf{J}$	source vector
m	mass
N	total number of cells
n	burning rate exponent
P_b	perimeter of gas column
p	gas pressure
R	gas column radius
R_g	gas constant
r_b	burning rate law
S	control surface
T	gas temperature
T_f	flame temperature
t	time
Δt	timestep
$\mathbf{U}$	vector of flow variables
u	axial flow velocity
V	control volume
x	axial location
Δx	cell width
Δx_{IF}	interface cell width
β	burning rate coefficient
γ	ratio of specific heats
$\epsilon^{(2)}$	second-order artificial viscosity term
$\epsilon^{(4)}$	fourth-order artificial viscosity term
$\kappa^{(2)}$	second-order artificial viscosity parameter
$\kappa^{(4)}$	fourth-order artificial viscosity parameter
ν	pressure variance term
ρ	gas density
ρ_{pr}	density of propellant

ACKNOWLEDGMENTS

I would like to thank my advisor Dr. Carl Knowlen for his guidance throughout this project and my time at UW. This research would not have been possible without his assistance and support. I also owe thanks to my fellow students who aided me during my time in the ram accelerator lab, including Trever Byrd, Ty Mundt, James Koch, Bryan Leege, Finn Van Donkelaar, and Kimmy Liu. I would also like to thank the University of Washington and U.S. Air Force for sponsoring me during this degree program. Lastly, I'd like to thank the incredible friends I've made in Seattle for supporting me through this program and ensuring I've played as hard as I've worked.

DEDICATION

to Mom, Dad, and Brock.

Chapter 1
INTRODUCTION

The ram accelerator is a hypervelocity launcher theoretically capable of muzzle velocities up to 12 km/s [1, 2]. The ram accelerator is essentially an in-tube ramjet. The projectile acts as the ramjet centerbody, the launch tube acts as the external cowling, and a premixed fuel-oxidizer mixture replaces the intake air and injected fuel. The projectile ram-compresses and combusts the stationary propellant gas to produce thrust. To achieve adequate ram compression, the projectile must enter the propellant gases at sufficient velocity. Typically, this requirement is met by accelerating the projectile with a light gas or conventional powder gun to 700-1200 m/s. Such methods can be expensive and subject the projectile to high accelerations. This thesis details the design and implementation of an onboard rocket that could reduce peak acceleration, peak barrel pressure, and cost per shot.

1.1 Ram Accelerator Background

1.1.1 Ram Accelerator Overview

The ram accelerator is a novel chemical method for launching projectiles at hypervelocities. Its chief advantage is the concentration of high pressure at the projectile base. In a powder or light gas gun, pressure is highest at the breech and decreases near the projectile. Sound speed of the driver gas limits projectile velocity, as the driving pressure waves cannot propagate faster than the sound speed. Additionally, launch energy is wasted accelerating the gas column behind the projectile.

The ram accelerator improves upon the conventional gun by establishing a high pressure

region that travels with the projectile. It operates using the same gasdynamic principles as a ramjet. The projectile travels through a tube filled with a gaseous fuel-oxidizer mixture. In the thermally choked ram accelerator (TCRA) mode, the projectile geometry generates shocks that decelerate the flow to a subsonic region behind the projectile where the fuel-oxidizer mixture combusts. The combustion products create a thermal choking plane aft of the projectile [3]. The illustration below in Figure 1.1 offers a comparison of ramjet and ram accelerator operation.

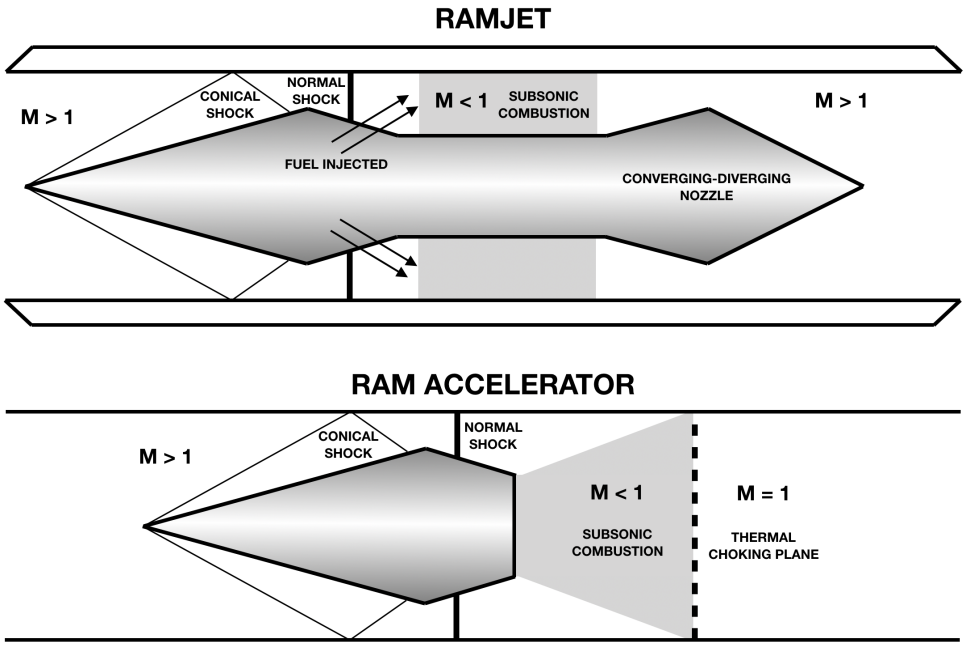

Figure 1.1: Diagram of conventional ramjet and ram accelerator.

Because the combustion zone travels with the projectile, the highest pressures occur at the base, yielding a nearly constant acceleration. Since the fuel and oxidizer are premixed, the ram accelerator avoids the fuel mixing issues ramjets face. These mechanisms facilitate high muzzle velocities across a range of bore diameters [1, 4, 5]. Other operating modes are possible, and using multiple stages tailored for specific velocity windows facilitates a smooth acceleration through a wide range of velocities [1, 2, 6].

Because the shock system and combustion rely on the relative gas velocity, the ram accelerator cannot accelerate a stationary projectile. In recent experiments, a high-pressure helium gas gun accelerated the projectile to 700-1000 m/s. The projectile entered an accelerator section, which contained the gaseous fuel-oxidizer contained at each end with Mylar diaphragms. A schematic of this setup is below in Figure 1.2.

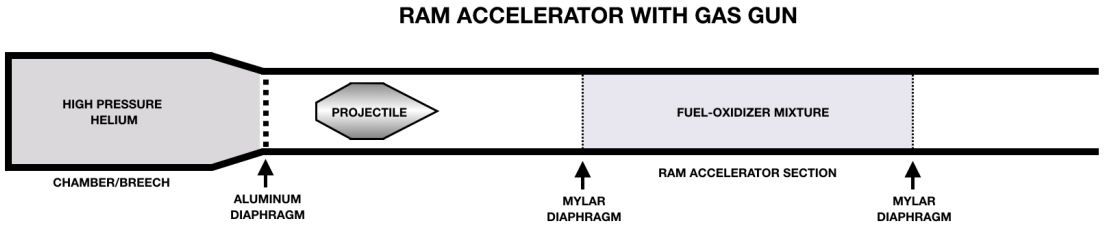

Figure 1.2: Diagram of current ram accelerator setup with helium gas gun.

1.1.2 Ram Accelerator Development

The ram accelerator has been thoroughly investigated at the UW facility and others [7]. The technology was originally developed at the University of Washington by Hertzberg et al. [1]. Successful ram accelerator operation was demonstrated, and an analytical model was derived using a quasi-steady, one-dimensional control volume. This model predicts the non-dimensional thrust based on the gas properties, propellant heat release, and projectile Mach number. Because each propellant mixture and fill pressure combination has a limited operation envelope, multiple driver sections with different compositions were combined, each separated by a diaphragm. Successive multi-stage operation was demonstrated by Bruckner et al. [3].

Further studies established operating limits of the thermally choked ram accelerator and characterized the nature of these limits both analytically and experimentally [8, 9]. Two mechanisms limit the ram accelerator operation window for a given Mach number and projectile geometry. When propellant heat release is too high, the normal shock on the projectile

is pushed forward past the projectile, decelerating it. This phenomenon is called a "wave unstart". The second phenomenon is "wave falloff", in which the normal shockwave moves back and falls off the aft of the projectile. Wave falloff occurs at low heat release, when there is insufficient energy to keep the combustion zone attached.

1.1.3 Ram Accelerator Applications

The ram accelerator has broad applications. A scaled-up version of the ram accelerator that could place a 2000 kg vehicle in a 500 km orbit was proposed by Bruckner [10]. Other studies have also investigated the viability of direct space launch [11, 12]. In these concepts, the ram accelerator would launch the vehicle at up to 10 km/s, imparting the majority of the requisite orbital velocity at launch. A small circularization burn would be required to complete orbital insertion. The ram accelerator has also been proposed as a kinetic energy weapon for defense applications [13].

Another application of the ram accelerator is as a hypervelocity test facility. Witcofski et al. suggested using the ram accelerator to launch instrumented payloads to test aerodynamic and aerothermal loads [14]. The ram accelerator offers better scalability and lower acceleration than other hypervelocity launchers [15]. Additionally, the ram accelerator is being privately developed for use in the mining industry [16].

1.2 Current Starting Requirements

1.2.1 Low Velocity Start

Schultz investigated the effect of entrance Mach and propellant heat release on the starting process [17]. He found that the ram accelerator started at Mach numbers 2.9-3.0 with fill pressures of 25-50 atm in CH_4-O_2-N_2 propellant. Typically, entrance velocity was on the order of 1150 m/s. This study was a preliminary investigation with no optimization for low velocity start.

Multiple efforts have been made to reduce the initial velocity requirements. Kruczynski

et al. [18] examined the effect of the obturator, gas mixture, and ignitor on low velocity start. The study identified a combination of stoichiometric CH_4/O_2 with CO_2 diluent and an obturator configuration that yielded successful operation at 760 m/s entrance velocity. Additionally, an effective pyrotechnic ignitor was demonstrated that ignited previously non-combusting mixtures, an important result for the onboard rocket implementation discussed later.

Knowlen et al. further explored low velocity start, adjusting CO_2 diluent concentration in a $1.5C_2H_6+2O_2+XCO_2$ mixture at 20 atm [19]. These experiments demonstrated mixtures that started with an entrance velocity of 700-800 m/s, though there was high sensitivity to diluent concentration. Projectiles in this study were started without the use of a pyrotechnic igniter.

1.2.2 Baffled Tube

All research mentioned thus far was performed on the smooth-bore ram accelerator. This designation signifies that the acceleration section is a smooth tube with a subcaliber projectile, typically equipped with centering fins. The baffled-tube ram accelerator (BTRA) is a modification that replaces the smooth accelerator section with a series of baffles or chambers separated by disks [20]. An illustration of the baffled tube is depicted below in Figure 1.3.

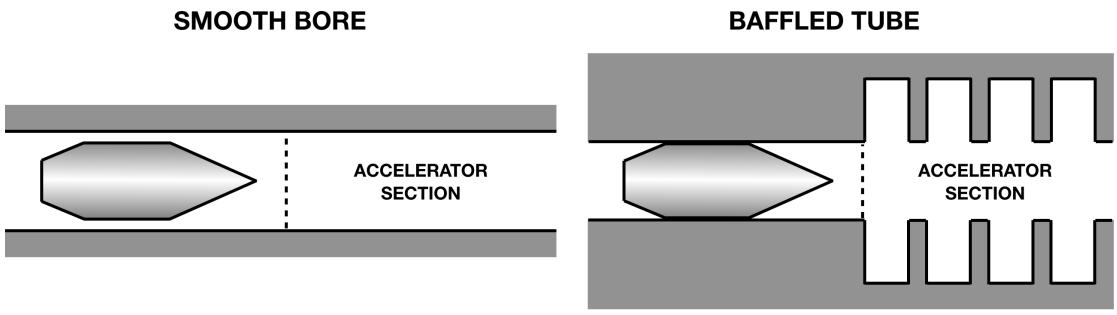

Figure 1.3: Comparison of smooth bore and baffled tube ram accelerator.

The baffled tube facilitates more energetic propellants, increasing thrust and performance

over the smooth-bore. The baffled tube also enabled the lowest velocity start achieved experimentally at 620 m/s. Additional studies by Knowlen et al. on inclined baffles (those with disks angled to the direction of travel) have not shown similar improvements in low velocity start, and further investigation into baffle optimization is required [21].

1.3 Current and Alternative Launch Schemes

1.3.1 Powder Guns

The powder gun is ubiquitous and is exemplified in firearms, cannons, and military artillery. In a powder gun, an explosive charge produces heated, high-pressure gases that accelerate the projectile. Figure 1.4 below is a diagram of a conventional powder gun. Powder guns offer the advantage of simplicity. The only mechanisms required are a firing pin to ignite the primer and an access door to load the projectile. The combustion only occurs in the breech, and propellants are often prepackaged in a shell. Disadvantages of powder guns include the heated combustion products, which can cause gun bore erosion and leave residue in the chamber [22]. In-service military powder guns are capable of launching projectiles as fast as 1220 m/s while experimental guns have reached muzzle velocities up to 3000 m/s. [23]. The Army Research Laboratory's 120-mm ram accelerator and Institut Saint-Louis's 90-mm facility both used conventional powder guns as their initial launchers [4, 24].

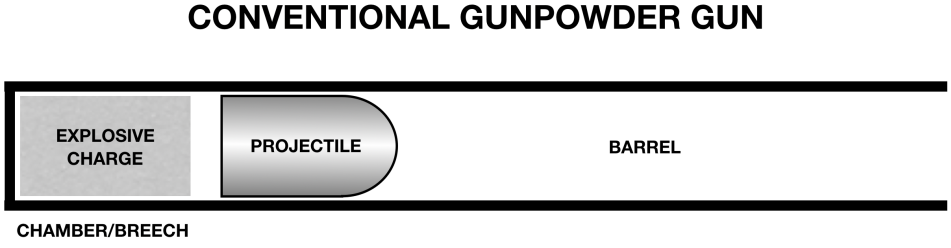

Figure 1.4: Diagram of conventional powder gun.

1.3.2 Gas Guns

Another design variant is the compressed gas gun. This design uses a chamber of pressurized gas to accelerate the projectile. A fast-acting valve or bursting diaphragm is used to for quick gas release. In powder and gas guns, a limiting factor for exit velocity is sound speed of the propellant gas. The gas gun offers the advantage of using low molecular weight propellant gases like helium or hydrogen, which are often lighter than the combustion products of powder guns. The University of Washington ram accelerator facility uses a compressed helium gas gun [25].

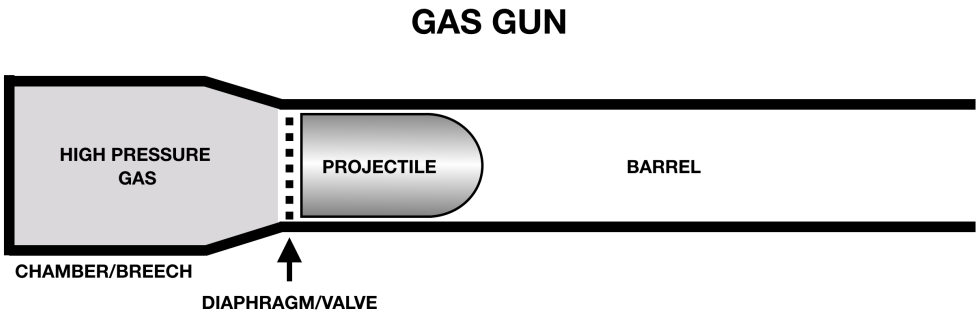

Figure 1.5: Diagram of gas gun.

1.3.3 Traveling Charge

The traveling charge concept was first introduced in 1947 by Langweiler (as cited in [26]). The traveling charge design augments the conventional powder gun design with a propellant charge on the aft end of the projectile. This end-burning charge burns at a high rate, generating impulse forces at the gas/solid interface and a high pressure region behind the projectile-propellant system [26]. Figure 1.6 depicts the improved pressure distribution of the traveling charge gun.

The impulse forces and localized high-pressure region provide improved efficiency over a conventional powder gun, especially at high charge-to-mass ratios [26]. The greatest chal-

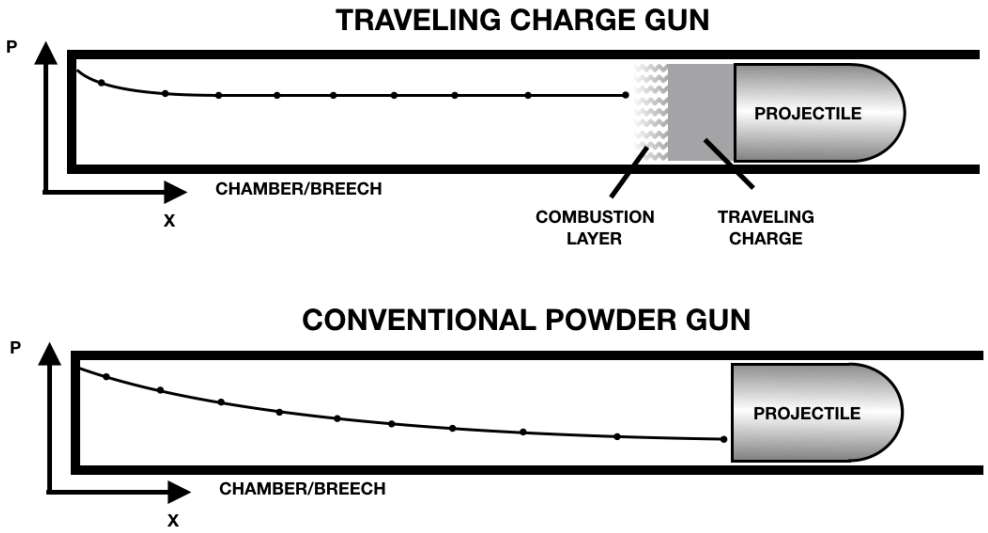

Figure 1.6: Diagram of traveling charge chamber pressure time history.

lenge with implementing the traveling charge concept is the burning rate of the propellant. Realizing the efficiency gains requires propellants with burn rates of hundreds of meters per second, while most propellants burn on the order of few centimeters per second. This technical gap led to the research and development of very high burning rate propellants, which had burn rates in experimental firings up to 1867 m/s [27]. More recently designs with porous, perforated, and liquid propellants have been developed [28, 29]. Though these technologies are promising, a conventional solid propellant rocket was used in this study for simplicity.

1.3.4 Releasing Gas Towards Projectile

In the aforementioned launch schemes, the projectile travels through the launch tube to enter a section of stationary propellant gases. An alternative is to accelerate the propellant gases towards the projectile. This design was originally investigated by Fisher who focused on filling the ram accelerator tube using unsteady gas dynamics [30]. Srulijes et al. investigated expanding shock tube gases combusting on a stationary test article [31, 32]. Hertzberg et al. filed a patent for a method of zero velocity start (ZVS) in which expanding propellant gases

from a shock tube flow over the stationary projectile and into a wave reflection disc [33]. The reflected shocks propagate downstream to the aft of the projectile, thereby heating the mixture to its ignition temperature and starting ram accelerator combustion. This design provides the requisite relative flow velocity and an ignition mechanism. The technique has only been investigated numerically by McFall et al. who calculated the expected performance at various conditions [34]. No successful experimental demonstrations of this launch method exist in the literature.

1.3.5 Rocket Launch Tube

In military and civilian applications, rockets are frequently launched from open tubes. The wall pressure distribution in the launch tube was modeled and measured first by Baston [35]. The model implemented a method of characteristics code, and experiments vented hot and cold gas jets in instrumented tubes of different lengths to simulate the flowfield while the rocket is at different stations. Further studies examined secondary flows including the impingement shock between the rocket and launch tube [36, 37, 38, 39]. While the models and results of these studies would seem applicable to the ram accelerator application, they examine an open-ended tube, which allows for quasi-steady analysis and different flowfield dynamics than the closed-tube case.

1.3.6 Solid Rocket Motors

Extensive research and modeling has been conducted on the internal dynamics of solid rocket motors. Early codes and techniques predicted chamber pressure, thrust, and specific impulse over time [40, 41, 42]. More recent research has included acoustic and stability analyses, propellant erosion models, and multi-dimensional models [43, 44, 45]. Quasi-one-dimensional (Q1D) models, which solve the Euler equations with varying area, have been shown to produce reliable results [46]. Q1D models have been solved with a variety of numerical schemes [46, 47, 48, 49]. This study used a second-order MacCormack scheme with artificial diffusion and fourth-order hyperdiffusion. Chakravarthy et al. used this scheme to evaluate acoustics

and stability in a solid rocket motor with non-smooth area variation [50]. This scheme was adapted to the case of a solid rocket in a launch tube by extending the computational domain to the area behind the tube, calculating the thrust, and dynamically moving the projectile and remeshing.

1.4 Project Overview

The ram accelerator is a useful method for launching projectiles at hypervelocities but requires initial velocities of at least 700-1200 m/s. Current methods use expensive helium or subject the projectile to high accelerations. An alternative launch scheme using an air gun and onboard solid propellant charge is proposed to reduce cost and peak acceleration. Such a design would be more cost effective for industrial and research applications and allow for less robust payloads.

A Q1D MacCormack scheme was developed for the solid rocket motor and in-tube gas dynamics. Static and in-tube tests were conducted to evaluate the accuracy of these models and the practicality of this launch method for the ram accelerator.

Chapter 2
THEORETICAL MODELING

Extensive modeling has been conducted on guns, ram accelerators, solid rocket motors, and rockets in an open-ended launch tube. However, no model for a rocket in a closed tube was found in the literature. A validated predictive model is important for future application of the onboard rocket in the ram accelerator. Existing quasi-one-dimensional schemes used in solid rocket motors provide sound models from which an appropriate model can be constructed.

2.1 Constitutive Equations

The Q1D Euler equations resemble the conventional 1D Euler equations but are adapted for varying cross-sectional area. This approach is common in the literature for solid rocket motors [45, 49, 48, 50, 46] and is simply extended to the problem of an in-tube rocket. Though various formulations exist for the Q1D equations, the form used here (Eqn. 2.1-2.3) most closely resembles those used by D'Agostino and Andrenucci [46]. Note that the combustion source terms are removed in cells without combusting propellant. A full derivation of these equations is available in Appendix A.

$$\frac{\partial(\rho A)}{\partial t} + \frac{\partial(\rho u A)}{\partial x} = P_b r_b \rho_{pr} \tag{2.1}$$

$$\frac{\partial(\rho u A)}{\partial t} + \frac{\partial\left[(\rho u^2 + p)A\right]}{\partial x} = p\frac{\partial A}{\partial x} \tag{2.2}$$

$$\frac{\partial}{\partial t}\left(\rho\left(e + \frac{u^2}{2}\right)A\right) + \frac{\partial}{\partial x}\left(\rho u A\left(e + \frac{u^2}{2} + p/\rho\right)\right) = r_b P_b \rho_{pr} h_f. \tag{2.3}$$

These equations were then put into vector form (Eqn. 2.4) for implementation in the MacCormack scheme. Important non-standard variables here include P_b - the perimeter of

the cell, r_b - the linear burning rate of propellant, ρ_{pr} - the density of solid propellant, and h_f - the specific enthalpy of the combustion products. Note the inclusion of the source term, $\mathbf{J}$, and pressure term, $p\,\partial\mathbf{A}/\partial x$, that differentiate this formulation from the conventional 1D Euler equations.

$$\frac{\partial}{\partial t}\mathbf{U} + \frac{\partial}{\partial x}\mathbf{F} = \mathbf{J} + p\frac{\partial}{\partial x}\mathbf{A} \tag{2.4}$$

where

$$\mathbf{U} = \begin{pmatrix} \rho A \\ \rho u A \\ \rho\left(e + \frac{u^2}{2}\right)A \end{pmatrix},\ \mathbf{F} = \begin{pmatrix} \rho u A \\ \left(\rho u^2 + p\right)A \\ \rho u\left(e + \frac{u^2}{2} + \frac{p}{\rho}\right)A \end{pmatrix},\ \mathbf{J} = \begin{pmatrix} P_b r_b \rho_{pr} \\ 0 \\ r_b P_b \rho_{pr} h_f \end{pmatrix},\ \mathbf{A} = \begin{pmatrix} 0 \\ A \\ 0 \end{pmatrix}.$$

2.2 Physical Assumptions

The gas was assumed to be ideal and calorically perfect. Heat loss to the tube walls and projectile was neglected. The combustion region was assumed to be a thin plane on the surface of the propellant charge. Combustion was assumed to be a function of pressure governed by the De Vielle-Saint Robert law:

$$r_b = \beta\,(p)^n$$

where r_b is the linear burning rate and β and n are empirically determined constants. More complete thermal and erosive burning models have been investigated elsewhere and provide areas of improvement for this model [43, 48, 45]. Friction between the launch tube and projectile was assumed to be negligible relative to thrust. Ignition was modeled as an instantaneous process that occurred at the beginning of the simulation or after a specified time delay. The flame temperature and properties of the combustion reaction were determined using NASA CEA [51].

2.3 Numerical Method

The computational domain extended from the interior of the solid rocket motor through the nozzle to the breech end of the launch tube. It was spatially discretized into 1D control volumes as depicted in Fig. 2.1. The system was solved using the second-order MacCormack technique [52]. Additional second-order diffusion and fourth-order hyperdiffusion terms were added to improve solution stability and reduce numerical oscillations, especially around shocks [53]. The projectile motion was predicted by calculating the net force on the projectile at each timestep and iterating the acceleration, velocity, and position accordingly. The net thrust was the sum of pressure forces and momentum flow through the nozzle. Full discussion of this implementation is available in Appendix A.

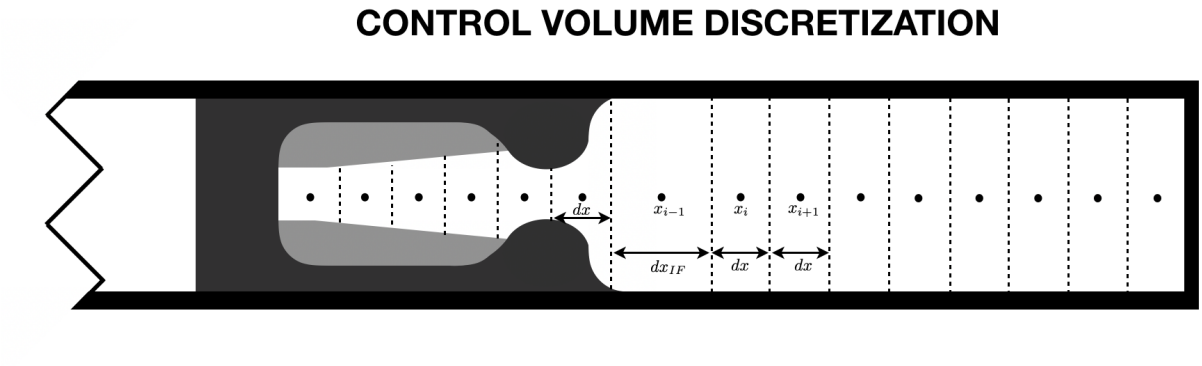

Figure 2.1: Spatial discretization of computational domain.

The mesh consisted of a projectile-fixed grid and tube-fixed grid connected by an interface cell, shown here as dx_{IF}. As the projectile moved through the tube, the interface cell was expanded, and when it was greater than twice the nominal cell size, a cell was added to the tube mesh. Thus, the computational domain could expand with the projectile without losing spatial precision. This code was easily adapted to the static fire test case by eliminating the launch tube section.

The artificial viscosity scheme as described in [53] provides numerical stability at high

Courant numbers and reduces numerical oscillation. Figure 2.2 demonstrates the effect of the fourth-order hyperdiffusion terms in Sod's shock tube problem [54]. The parameters for the second- and fourth-order diffusion are $\kappa^{(2)}$ and $\kappa^{(4)}$ respectively.

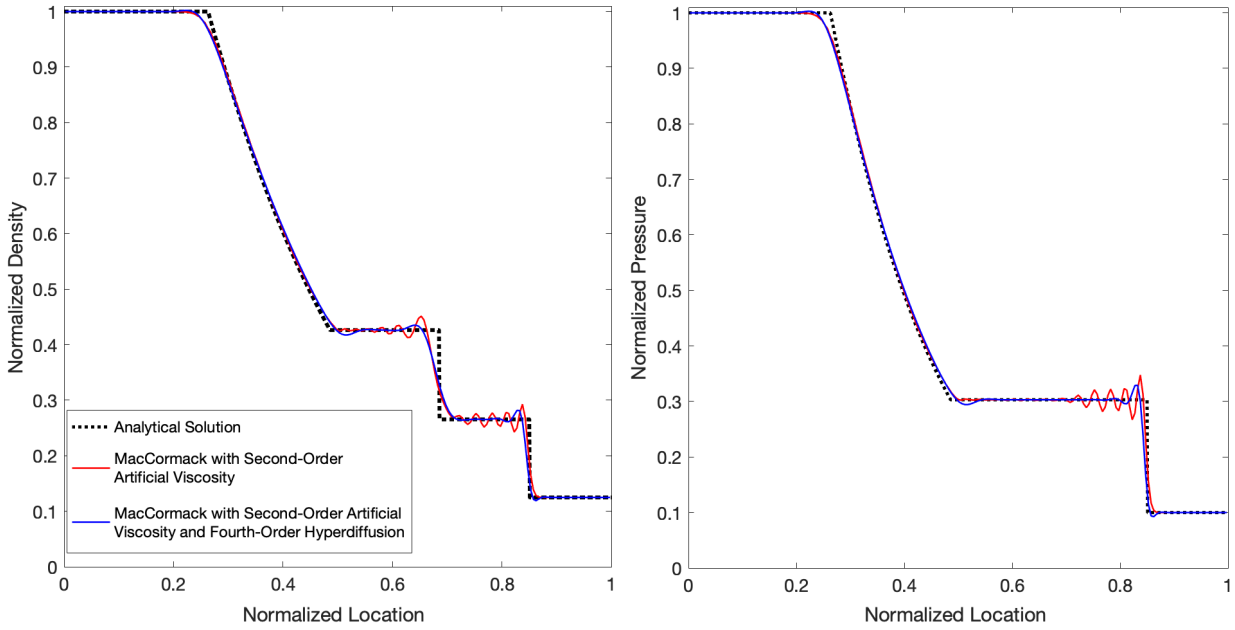

Figure 2.2: Sod's shocktube solution at $t = 0.2$s for $N = 200$, C $= 0.2$, $\kappa^{(2)} = 0.25, \kappa^{(4)} = 0.05$.

The timestep Δt was calculated in the method outlined by Anderson [52]. The local flow and sound speed in each cell were denoted as u_i and a_i. The local timestep is then defined by

$$\Delta t_i = C\left(\frac{\Delta x}{|u_i| + a_i}\right)$$

where C is the Courant number. A uniform timestep of $\Delta t = \min\left(\Delta t_i\right), i = 1, 2, ..., N$ was then selected and used for the successive iteration.

The Q1D model was used for two distinct cases. The first case was the static fire, in which the solid rocket motor fired with no enclosure or conditions imposed at the nozzle. This scenario allowed experimental verification of the thrust profile and chamber pressure.

The second case was the in-tube firing, in which a compressed gas gun launched a projectile with an onboard solid rocket motor. The initial launch propelled an inertial firing pin into a percussion cap, which ignited the motor. Both cases were important for evaluating the Q1D model and provided an experimental basis for implementing this technology in the ram accelerator.

Chapter 3
EXPERIMENTAL PROCEDURES

This chapter details the experimental procedures used to test the Q1D model of the solid propellant charge. Both static and in-tube tests were conducted to evaluate the model. The experiments were conducted in the University of Washington Ram Accelerator Lab.

3.1 Static Test Fire

Initial experiments were conducted on a static-fire test stand to evaluate the performance of the packed blackpowder rocket. The test article was an aluminum combustion chamber with a brass cap/nozzle insert. This aluminum chamber included a port for a pressure transducer. Pressure and thrust profiles were recorded. The combustion chamber was placed on a thrust stand equipped with a load cell. A diagram of this setup is pictured below in Fig. 3.1.

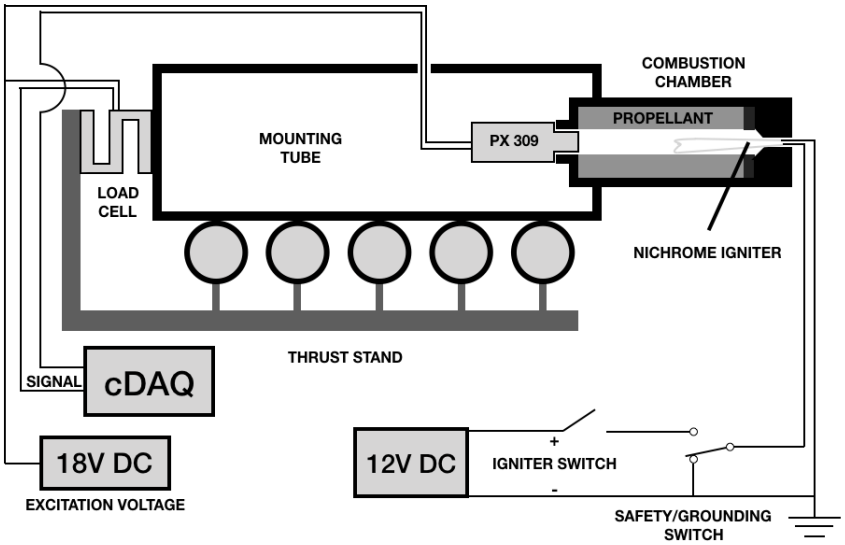

Figure 3.1: Diagram of static thrust stand setup and instrumentation.

The blackpowder was packed in a hollow cylindrical charge along the perimeter of the chamber using the process depicted in Fig. 3.2. A metal cylinder of the same diameter as the charge interior was placed in the center of the chamber, leaving a concentric tubular cavity into which the proper mass of blackpowder was poured (A). A tubular insert and retaining washer were then inserted into this cavity and pressed to pack the powder (B). The inserts were removed leaving the hollow cylindrical charge (C).

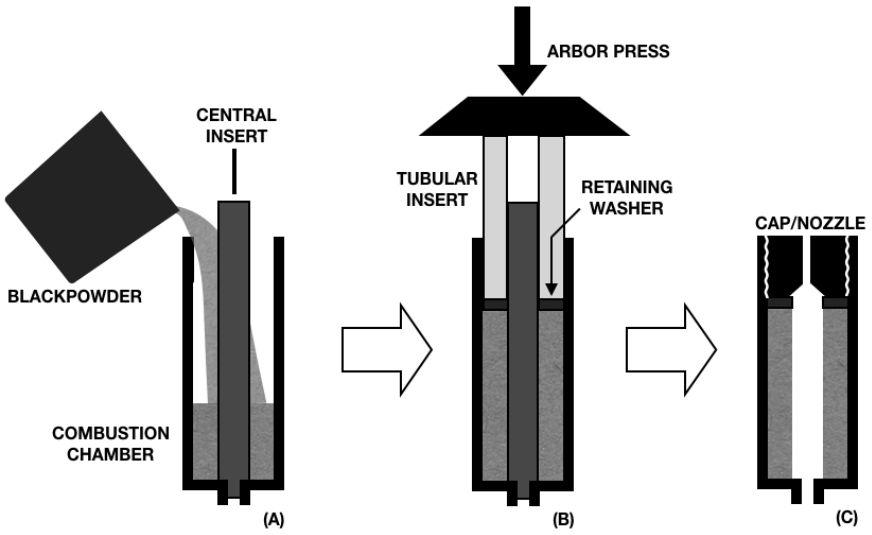

Figure 3.2: Procedure for packing black powder charge.

A brass nozzle was inserted into the open end of the combustion chamber, and the motor was fixed to the test platform. An Omega PX319-3KG5V pressure transducer and a Calt DYLY-103 30KG Load Cell were connected to a National Instruments NI cDAQ-9174 compact DAQ. A MATLAB program connected to the NI DAQ system collected pressure and thrust data at 1 kHz. A nichrome ignitor inserted into the nozzle was used to ignite the powder. A 3D rendering and technical drawing are below in Fig. 3.3.

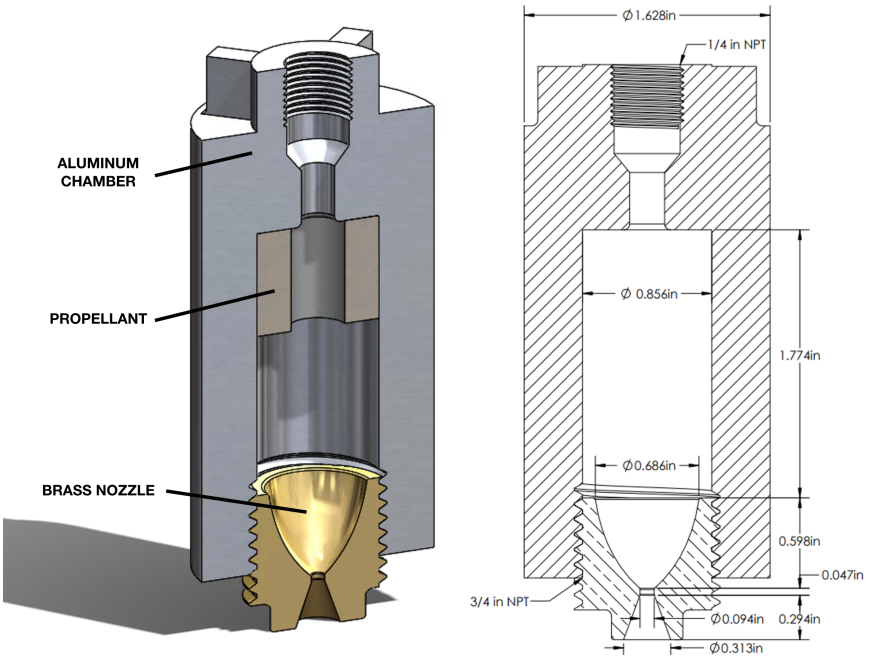

Figure 3.3: Static fire solid rocket motor.

3.2 In-tube Projectile Test

3.2.1 Projectile

To test the in-tube dynamics, a projectile with a solid propellant charge was manufactured. The projectile included a brass combustion chamber and inertial firing pin, a percussion cap, and a polycarbonate body. A cross-section of the design is below in Figure 3.4 and full technical drawings are available in Appendix B.

The blackpowder was packed into the combustion chamber using the same method discussed above. The projectile was assembled in the configuration depicted in Fig. 3.4. CCI small pistol primers were used as percussion caps, and Goex FFFF blackpowder was the solid propellant. A breakwire was tied to the firing pin and epoxied to the cap of the projectile. The breakwire was sized to break upon the initial acceleration from the compressed gas. The firing pin accelerated towards the percussion cap, striking and firing it. Additionally, two

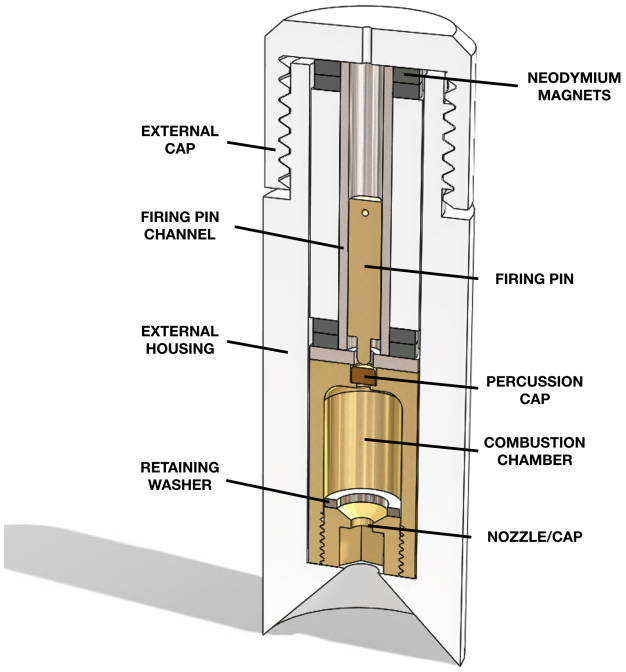

Figure 3.4: Cross-sectional view of projectile design.

launches were ignited electrically with a nichrome ignitor in an evacuated tube. The aft end of the projectile featured a chamfered section which formed a seal against the launch tube upon pressurization. The projectile also included two neodymium magnets which were used for location and velocity detection.

3.2.2 Projectile Design and Structural Analysis

The Q1D model was used to predict the loads on the projectile. The breech pressure was assumed to be 1000 psi, and the combustion chamber had a hollow cylindrical packed black-powder grain. The combustion chamber was assumed to be 200 g and constructed of UNS C26800 yellow brass. This material has a yield strength of 97 MPa and ultimate tensile strength of 315 MPa. From the model, the chamber pressure was predicted to be 10 MPa. This pressure was applied using a finite element analysis (FEA) tool in Ansys 19.1. The result from this FEA is below in Fig. 3.5. The maximum equivalent stress was 42.5 MPa.

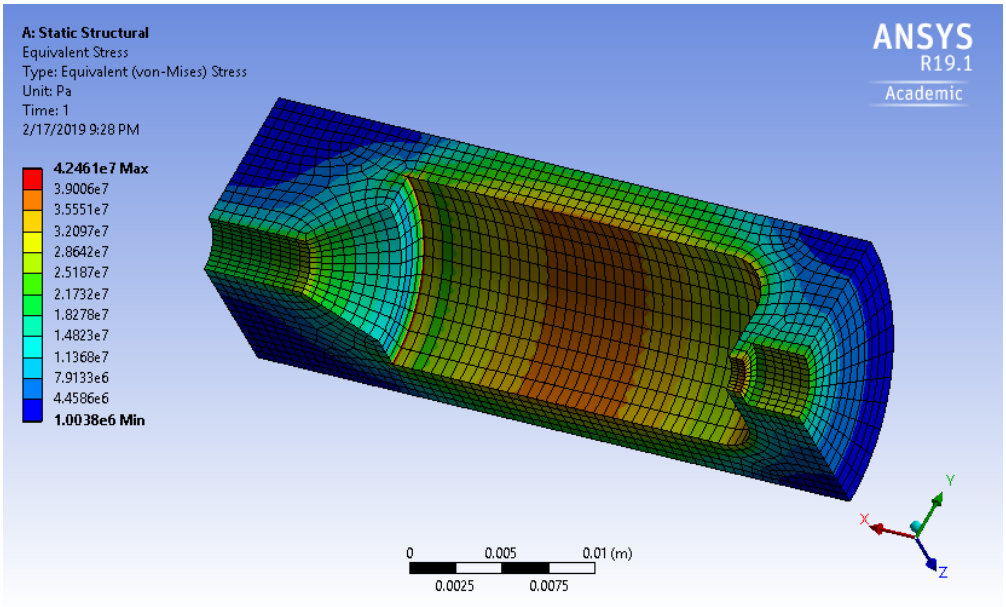

Figure 3.5: Ansys 19.1 FEA of combustion chamber for in-tube test article.

3.2.3 Static Timing Test

A static test was performed on the projectile's firing pin and primer ignition system to measure the time between firing pin strike and propellant ignition. The test rig is depicted below in Fig. 3.6. It included an enclosure for the brass combustion chamber and washer, a channel for the firing pin, an electrical timing plate, and a luminosity probe. Tests were conducted by packing 2.5g of black powder into the combustion chamber and installing the chamber, nozzle, primer, washer, and firing pin in the test rig in the same configuration as inside the projectile. A fiber optic cable was installed at the nozzle and connected to a photodiode. A small sheet of metal was placed such that the hammer would contact it upon firing. An RC circuit attached to the metal and plate generated a voltage upon contact. This trigger voltage and the photodiode were connected to a PXIc-1071 bus operating at 50kHz. Data recording was triggered using the trigger voltage from the contact plate, and 50,000 samples were recorded. Additionally, video was recorded using an iPhone XS at 240Hz.

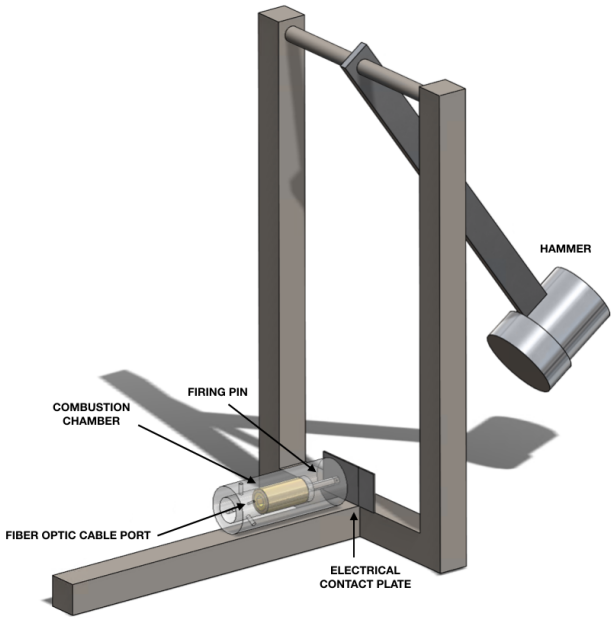

Figure 3.6: Static test stand for timing tests.

3.2.4 Test Facility

The in-tube tests were conducted in the UW ram accelerator lab. Traditionally used for ram accelerator experiments, the facility offered ample instrumentation and launch capabilities for the in-tube tests. A diagram of the test facility is below in Fig. 3.7. In the typical setup, a compressed gas gun (pictured at left) is used to launch projectiles through the instrumented test section into the exit dump tank and catcher tube. For these experiments, the 16m test section was isolated with 3/8in steel plates. The test section consisted of eight 2m subsections, which were each equipped with five equidistant instrumentation stations. Each station had two to four instrumentation ports available for electromagnetic (EM) sensors or piezoelectric pressure transducers (PCBs). The EM sensors detect the neodymium magnets onboard the projectile as it passes by using a coiled wire. A full explanation of the EM sensors is available in Ref. [55]. This facility used a National Instruments PXIc-1071 bus operating at 200 kHz with 32 channels for data acquisition. The system recorded 50,000

samples from 19 EM sensors and the wall pressures from 12 PCBs. Data recording was triggered by the first PCB sensor after the breech, and 10,000 samples were recorded before the trigger.

The 16m test section was separated from the 2m breech using two 0.014in thick Mylar diaphragms which were sized to burst at approximately 1000psi. The 6m braking section was filled with 50-150psi of nitrogen and isolated with a 0.005in thick Mylar diaphragm. In the braking section, the projectile acted as a piston, compressed the braking gas, and eventually reflected back towards the breech and stopped. Before each shot, the test section was pumped to vacuum.

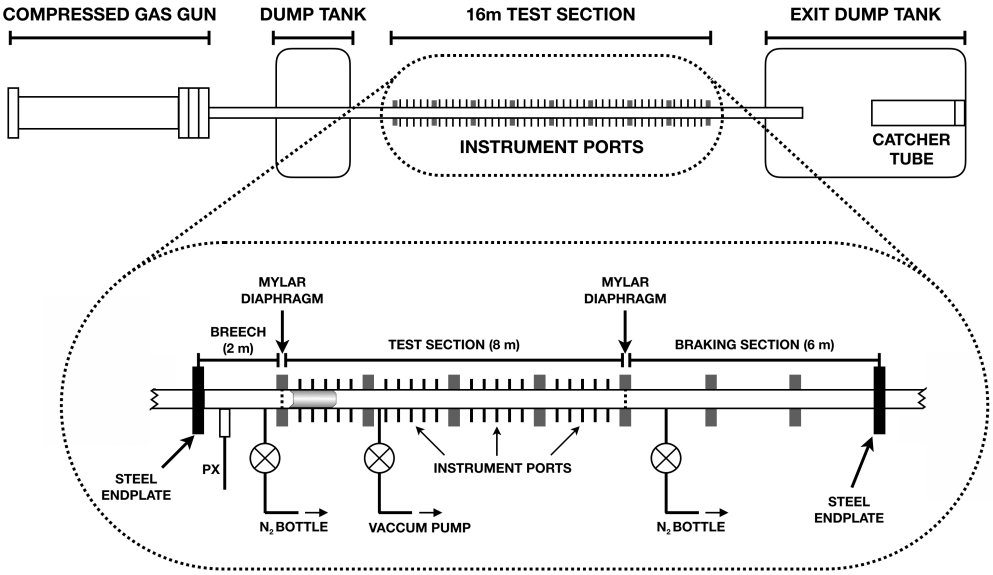

Figure 3.7: UW ram accelerator facility.

3.2.5 Experimental Procedures

The combustion chamber was packed with blackpowder using the method detailed in Fig. 3.2. The retaining washer and nozzle were inserted, and the projectile was assembled in the configuration shown in Figure 3.4. A thin wire was tied through the hole in the firing pin,

pulled through the hole in the external cap, and epoxied to the front face of the projectile. This wire fixed the firing pin to the end of the channel and was sized to break upon initial acceleration. The projectile was loaded into the launch tube, and the Mylar diaphragms were installed. The braking section was filled to the requisite pressure with nitrogen, and the breech was pressurized until the Mylar diaphragms burst and the projectile launched. The pressure and magnetic data were recorded, and the projectile was extracted.

Chapter 4

RESULTS

This chapter discusses the results of various tests conducted to evaluate the model of onboard solid rocket. A mesh refinement study was conducted on the Q1D model to ensure adequate spatial resolution. Additionally, static experiments were conducted on two different test stands to measure the chamber pressure, thrust, and ignition delay of the solid rocket. The test projectile was also launched in the UW ram accelerator facility to examine in-tube effects.

4.1 Mesh Refinement Study

To evaluate the effect of grid size on the Q1D theoretical model, a mesh refinement study was conducted on the static fire case, but with area change from propellant burning neglected, so a steady-state solution could be found. The cell sizes tested were 1mm, 0.75mm, 0.5mm, 0.25mm, 0.125mm, and 0.0625mm. Convergence was defined as an average pressure variation between timesteps of less than 1 μPa. The simulation parameters were CFL $= 0.1, \kappa^{(2)} = 0.25$, $\kappa^{(4)} = 0.01$. Sections of the grids tested are displayed in Figure 4.1.

The static fire case was considered due to its smaller computational domain and ease of comparison. Figure 4.2a displays the pressure as a function of axial location for each case, and Figure 4.2b is the converged chamber pressure as a function of number of cells. Convergence is evident at cell sizes 0.25mm or less, though no significant difference occurs at the smaller 0.125mm or 0.0625mm cells. These computational results indicate that a cell size of 0.25mm or smaller is required for simulations at this scale.

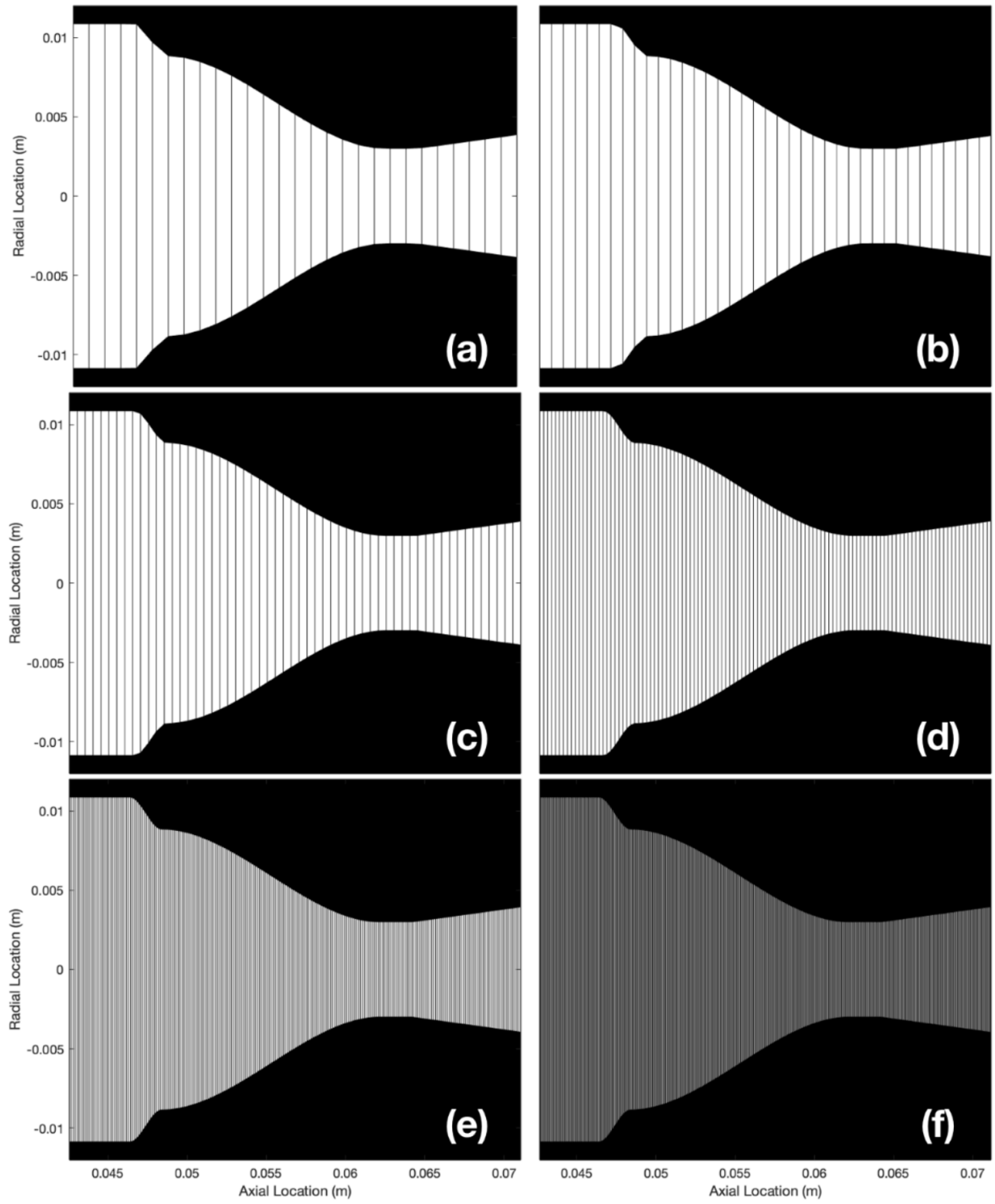

Figure 4.1: Comparison of Q1D meshes of static fire solid rocket motor: a) $\Delta x = 1$mm, a) $\Delta x = 0.75$mm, a) $\Delta x = 0.5$mm, d) $\Delta x = 0.25$mm, e) $\Delta x = 0.125$mm, f) $\Delta x = 0.0625$mm.

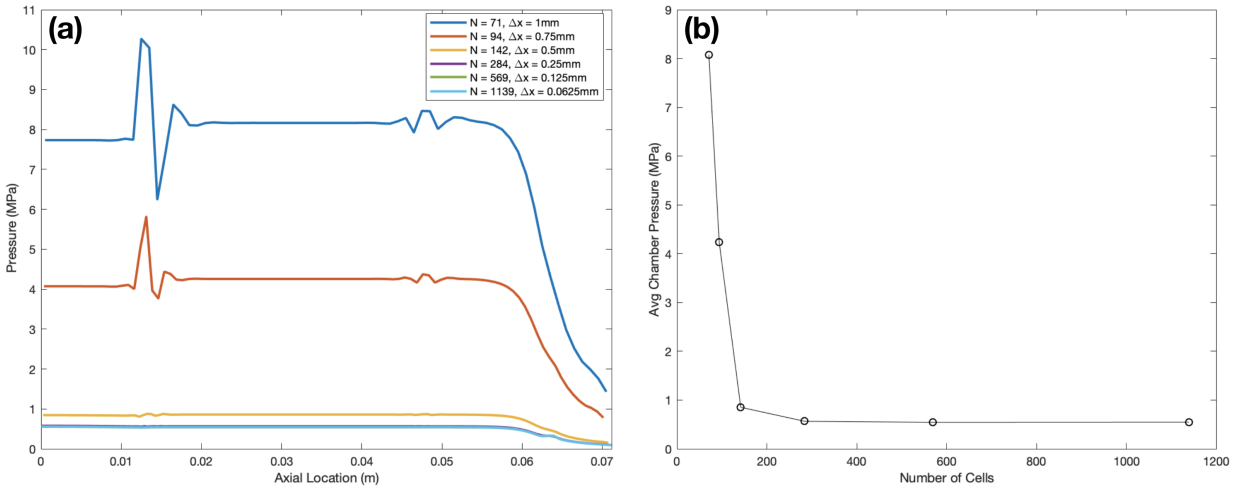

Figure 4.2: (a) Converged pressure distribution and (b) convergence plot of Q1D mesh.

4.2 Static Experiment

Three static test fires were executed to evaluate the accuracy of the Q1D model. A pressure transducer recorded chamber pressure, and a load cell recorded thrust. The profiles for each variable are below in Figures 4.3a and 4.3b. In all but one case, the pressure transducer was saturated, which is evident in Figure 4.3b. Precise ignition time was not obtainable due to inconsistent heating times for the nichrome ignitor, so the profiles here are aligned by peak thrust.

Two results from the Q1D model are also included. The first, denoted by the dashed line, is the theoretical prediction for the pressure and thrust. The second is the same theoretical model but with a burning rate coefficient of $12.5 \times \beta$. This adjustment was made to account for the suspected fracturing or disintegration of the propellant charge upon pressurization. This phenomenon was predicted because of the short observed burn time of approximately 0.01s or 10ms. The linear burn rate of blackpowder from pressures of 1 MPa to 25 MPa is 2-4 cm/s. The thickness of the hollow cylindrical charge was approximately 6mm, so the expected burn time should have been 150-300ms, fifteen to thirty times longer than the

observed burn time. These results indicated an inaccurate burning model, so a theoretical model with a dramatically increased burning rate was included to account for the increased burning area that would result from propellant fracturing.

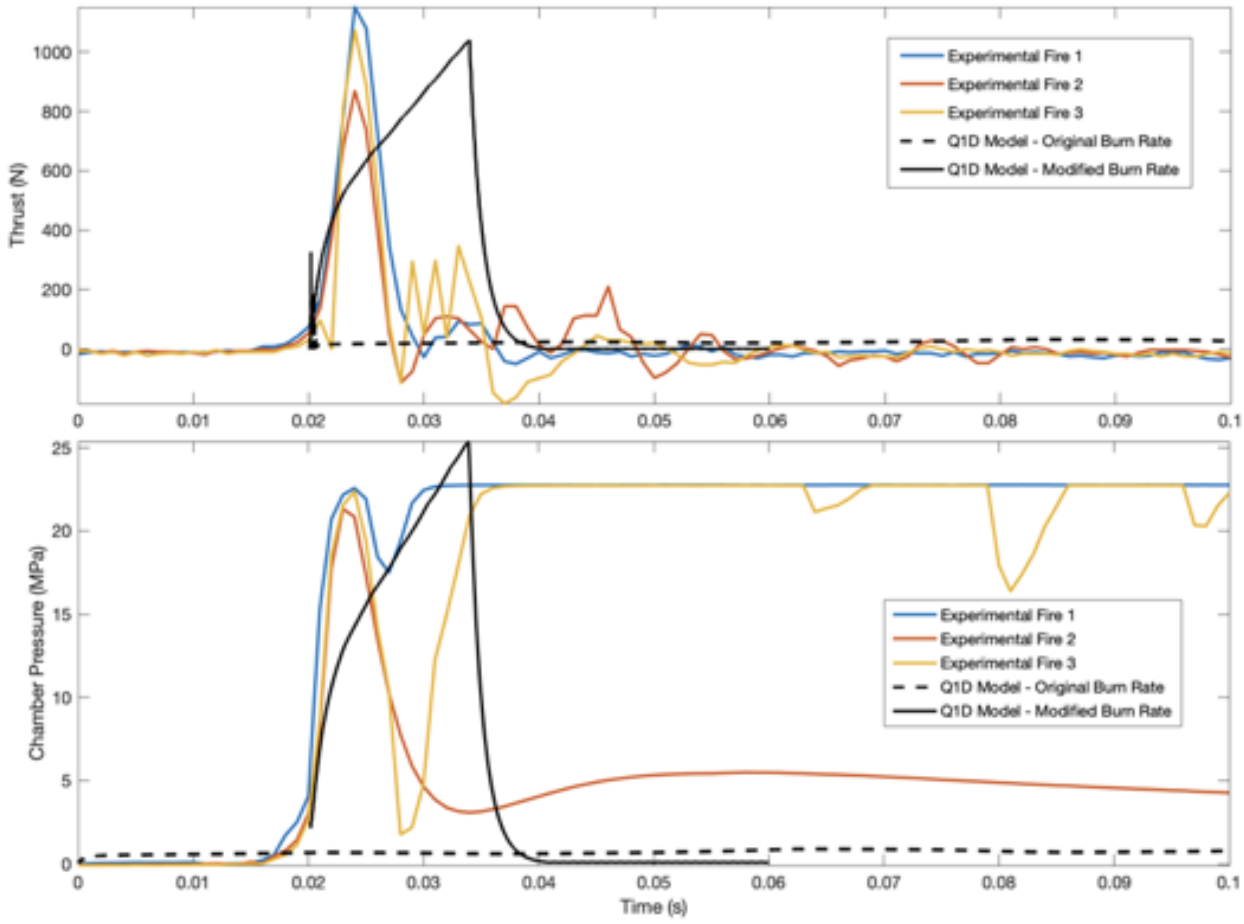

Figure 4.3: Thrust (a) and chamber pressure (b) from static thrust stand.

The modified Q1D model indicated a slower pressure rise than was recorded in the experiment with a greater peak. Additionally, the thrust data appears to include oscillations from the mounting tube reverberating after the initial thrust peak. Only one non-saturated pressure profile was recorded, though some hysteresis is suspected as the post-peak pressure was sustained at 5 MPa despite the thrust falling to zero.

4.3 Timing Experiment

The static test fires did not allow collection of precise timing data, so a separate experiment was conducted to determine the delay time between firing pin movement and ignition. A test stand was constructed that held the projectile's combustion chamber and firing pin in the design configuration. A hammer swung and struck the firing pin and a thin metal plate fixed to it, completing a circuit and generating a voltage which was recorded. A fiber optic cable was fixed at the nozzle and connected to a photo diode to record luminosity data. Video at 240 MHz from an iPhone XS was used to confirm the timing data. Three trials were conducted, but luminosity data was only recorded in one experiment. The voltage across the electrical contact and the uncalibrated luminosity voltage are displayed below in Fig. 4.4.

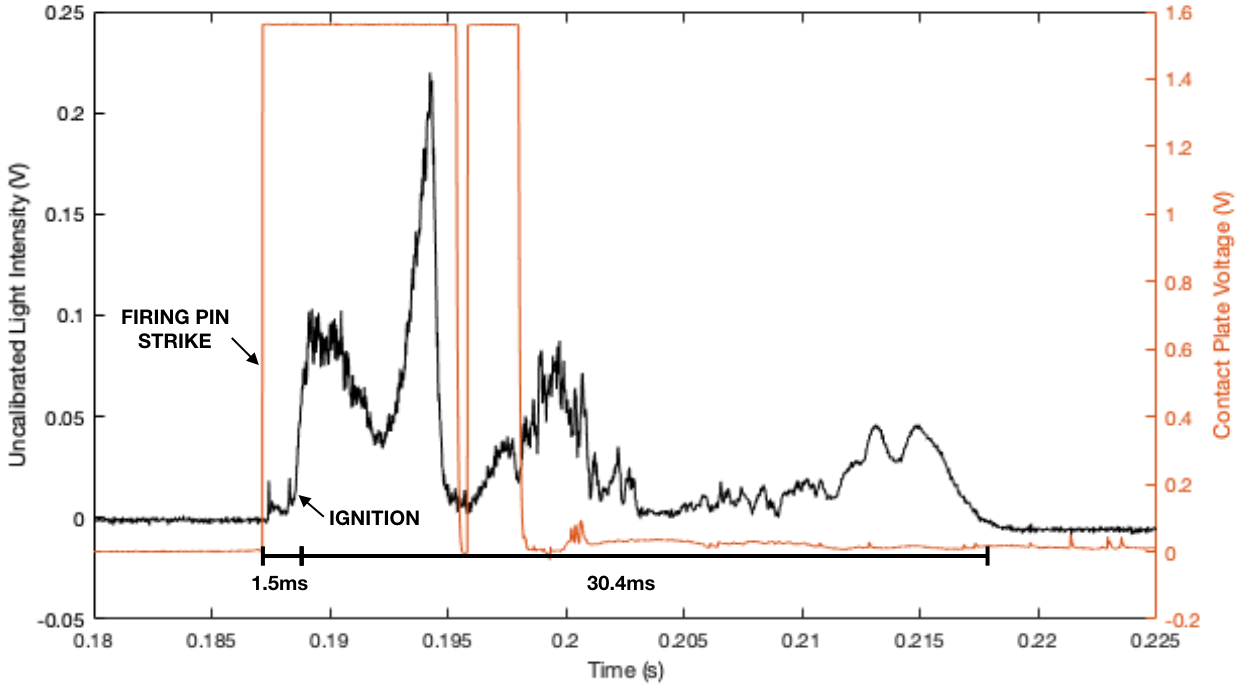

Figure 4.4: Electrical contact time and uncalibrated light intensity profiles over 45ms window.

The initial 1.5ms window between firing pin striking and significant light intensity increase was assumed to be the ignition period. The low-intensity light recorded in this window

was likely from the primer combustion. The full burn time was 30.4ms as measured by the luminosity probe, which was supported by the videos. Frames from the videos for each of the three firings are below in Fig. 4.5. The third row of photos is the experiment corresponding to the luminosity data in Fig. 4.4. The temporal resolution of the video and residual sparks and smoke prohibit precise timing, but the videos support the findings of the luminosity probe. Ignition occurs within one frame (4.2ms) and flames are visible for 5-8 frames (20.8-33.3ms).

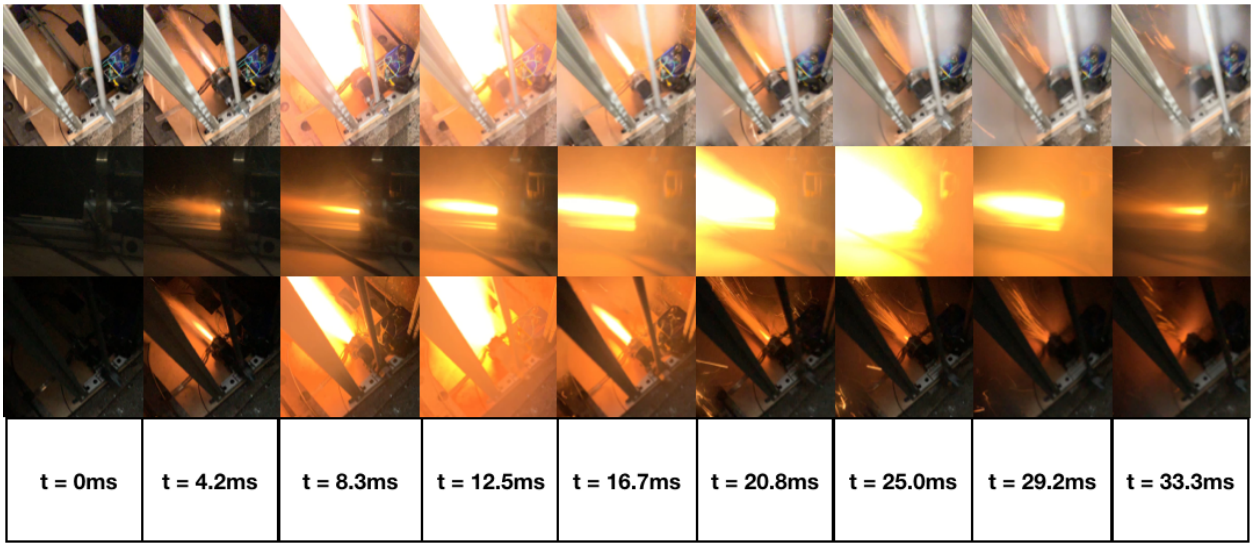

Figure 4.5: Frames from 240Hz videos taken with iPhone XS.

4.4 In-tube Experiment

In-tube experiments consisted of two inert shots with a polycarbonate cylinder to test instrumentation and act as a control case. Additionally, two "hot" shots were performed in which the projectile was launched by the pressurized breech and the inertial firing pin ignited the propellant. Two more shots were conducted with an evacuated launch tube and electrical ignitor. These tests provided an array of conditions against which to test the Q1D model.

4.4.1 Inert Experiments

Two launches were conducted with a 226g polycarbonate cylinder equipped with a single neodymium annular magnet. The same launch procedure was used for these shots as for the rocket projectile. Data for the shot are below in Fig. **??** and are compared to a Q1D simulation of a 240g projectile launched with 1000psi breech pressure. The actual recorded breech pressures for the inert shots were 1086psi and 1075psi respectively. The data matches the model well until approximately 9.5m where the blow-by gases start decelerating the projectile before the diaphragm at 10m. The Q1D model predicts slightly lower velocities than those observed which is expected, as it modeled a heavier projectile with lower breech pressure. This comparison provides confirmation of the gasdynamic accuracy of the Q1D model without combustion.

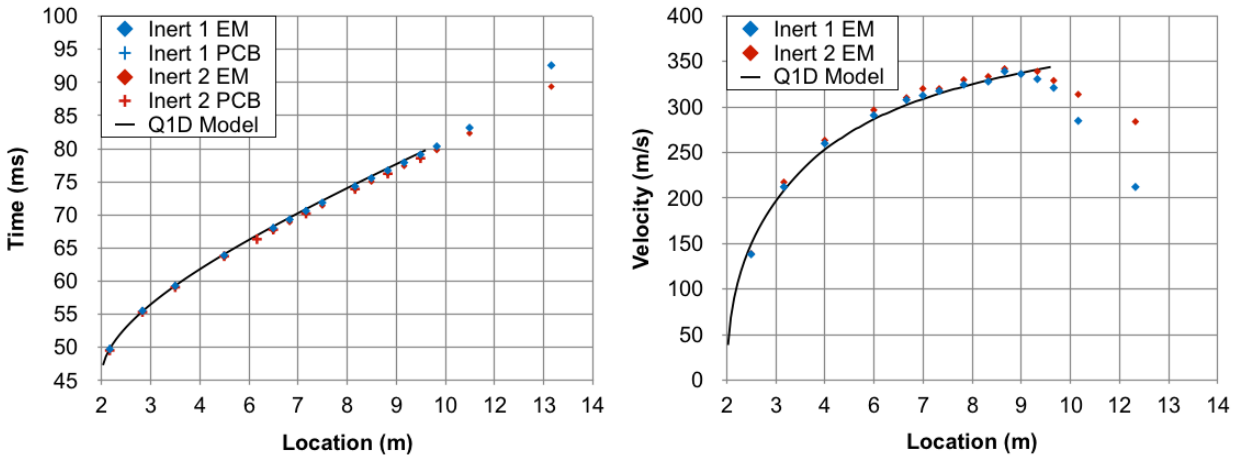

Figure 4.6: Motion data from the inert slug shots and Q1D simulation.

4.4.2 Rocket-Only Experiments

Two experiments were conducted with the rocket projectile in an evacuated tube and no gas gun. The rocket was ignited electrically with a nichrome ignitor, and the projectile was placed at 2m or 5cm from the endwall. These tests were intended to evaluate the modeling

of combustion product gasdynamics without the interference of the gas gun. Additionally, the static launch capabilities of the rocket were evaluated. Data from these two shots are displayed below in Fig. 4.8. For these tests the projectile was equipped with two annular magnets, which allowed for single point velocity data to be measured. Both single-point and the conventional multi-point EM sensor velocities are displayed. The Q1D model predicted far higher velocities in the time window than those observed, indicating inaccuracies in the combustion model or combustion product gasdynamics. However, the projectile was able to attain a velocities of 33m/s and 82m/s with a propellant mass fraction of 1.04%. Constraining the rockets within the tube increased equivalent specific impulse to 322s and 804s respectively, a dramatic increase from black powder's typical 80s specific impulse.

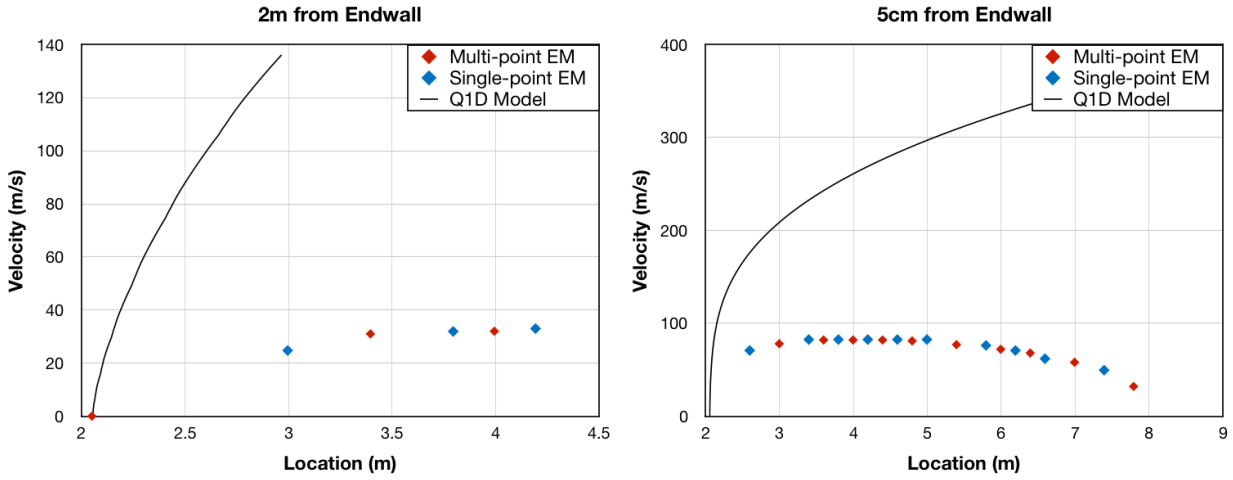

Figure 4.7: Motion data from rocket in evacuated tube and Q1D simulation.

4.4.3 Rocket Augmentation Experiments

Two experiments were performed with the rocket projectile operating as designed with initial launch by compressed gas gun and ignition by the inertial firing pin. These two shots had breech pressures of 1085psi and 882psi. Ignition of the propellant charge was confirmed by inspection after each shot. Below is a velocity diagram for these rocket augmented shots as

well as comparison with inert shots and theory. According to the model, the rocket should have added an additional 80m/s of velocity by the end of the test section but no such effect was found.

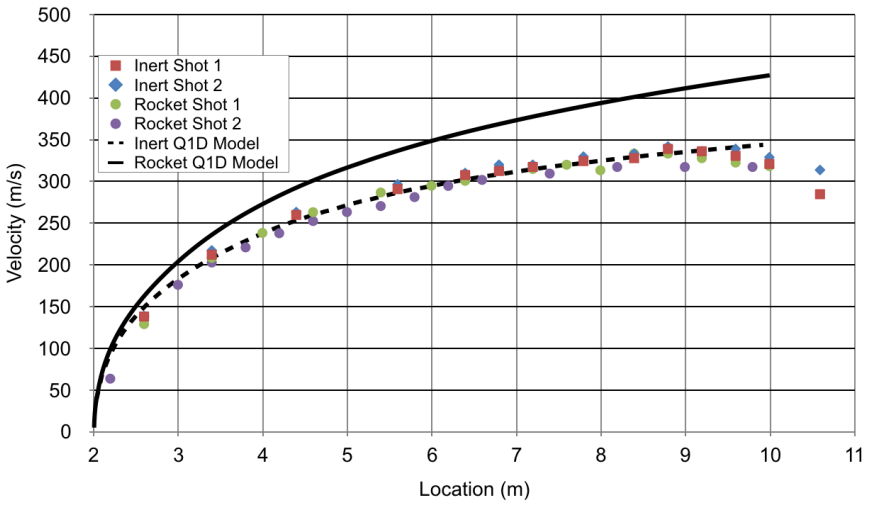

Figure 4.8: Motion data from rocket augmented projectile and Q1D model.

Chapter 5
DISCUSSION

The ram accelerator is capable of launching projectiles at high muzzle velocities but requires a supplementary initial launcher for operation. Existing ram accelerators use single-stage light gas guns or conventional powder guns. These techniques impart high peak accelerations and require high breech pressures. An onboard solid propellant rocket coupled with a lower pressure air gun was proposed to replace these techniques with the aim of reducing cost and peak acceleration.

A Q1D model was developed and implemented to calculate the gasdynamics and motion of a rocket-equipped projectile. The Q1D model was evaluated for both a static fire and in-tube test case in the UW ram accelerator lab. Thrust and chamber pressure profiles were generated from the static case, and motion and launch tube pressure data were recorded for the in-tube case.

5.1 Conclusions and Analysis

A mesh refinement study was conducted to determined the proper cell size for these cases. The static fire setup was used with a constant area profile, and the solution was iterated until convergence. The mesh refinement study indicated that a cell size 0.25mm or less was required. While this analysis was sufficient for these experiments, a non-dimensionalized convergence study would have been ideal. Step size could be defined as a fraction of minimum or local diameter. Such results would be more generalizable to other Q1D cases.

Three static timing tests were completed with usable luminosity data only collected from one. The light intensity profile indicated that ignition occurs approximately 1.5ms after firing pin strike and the burn time was 30.4m/s. These results were confirmed by the video of all

three tests. The short ignition and burn time ensure that combustion is completed within the test section of the launch tube. The projectile was in the test section for approximately 33ms during launches with the compressed gas gun. These tests also confirmed the viability of the firing pin/primer ignition technique.

Three successful static fire experiments were executed. The thrust and pressure peaks were dramatically higher than those predicted by the Q1D model. This discrepancy is likely due to an incomplete burning rate model. The burning rate model does not include erosive burning effects or the propagation of the flame front into the porous propellant. The integrity of the solid propellant is also unknown, and it is possible the charge fractured or disintegrated upon chamber pressurization, increasing the surface area and generating a short, sharp pressure peak. Comparison of data with a modified burn rate model indicates that the observed pressure and thrust were consistent with a burn rate 12.5 times that predicted. Experimentation with alternate, stronger propellants such as ammonium perchlorate is recommended to further evaluate the accuracy of the Q1D model. Additionally, a pressure transducer with higher range is recommended for future testing, as transducer saturation was evident in two of three experiments.

Six in-tube tests were accomplished: two inert shots, two electrically ignited shots, and two rocket augmented gas gun shots. The inert shots were executed with a 226g polycarbonate slug and confirmed operation of the tube instrumentation. The shots also confirmed the validity of the inert gasdynamics of the Q1D model. These results indicate that the discrepancies between theory and experiment in other trials are likely due to inaccurate combustion models.

Two shots in the evacuated tube were used to evaluate the rocket independently of the compressed gas gun. The projectile was placed at 5cm and 2m from the end wall. While the rocket attained speeds of 82m/s and 33m/s respectively, these velocities were far lower than those predicted by the Q1D model. These results confirm the discrepancies observed in the static test between the combustion model and experiment. However, these tests provide valuable data against which improved models can be developed. Blow-by gases were also

suspected to reduce launch velocity, as the projectile sustained damage from protruding instruments, compromising its ability to seal against the tube walls.

Two rocket augmented shots were also executed. These shots did not produce the velocity increase predicted by the Q1D model, though the inert shots do not provide adequate comparison to conclude that the rocket had no effect. The inert shots used a lighter projectile, and tube friction and blow-by gases could have also varied. Additionally, only inert shot 2 and rocket shot 1 had the same breech pressures, and all others varied by up to 200 psi. Further experimentation is required to isolate the effect of the rocket, but the results of this study did not find significant improvement in launch velocity.

Q1D models used in other studies of solid rocket motors typically simulate conventional solid rocket propellants such as ammonium perchlorate. These propellants have more predictable burning characteristics than black powder and face less risk of fracturing. Additionally, the energy addition by the black powder predicted by the model was far higher than that observed. These results could be due to incomplete combustion or inaccurate prediction of combustion heat release. The inert gasdynamic simulation of the Q1D model is well supported by the results from the inert slug shots, so correction of these two mechanisms would likely yield an accurate model. Regardless, the experiments in this study do not indicate significant improvement using rocket launch augmentation.

5.2 Suggestions for Future Research

The results of this study indicate room for significant improvement of the Q1D model. Alternative propellants are suggested, as well as in-house burning rate tests using the propellant and packing procedures used in the rocket. Such experiments could likely identify any fracturing or structural degradation of the propellant grain. Furthermore, experimentation on the heat release of the blackpowder under these combustion conditions would provide useful data to check thermodynamic assumptions of the model.

The effect of the rocket could be isolated with further experiments using existing equipment. An inert shot with the rocket projectile at the same breech pressure as existing rocket

shots would allow direct comparison between the cases and provide valuable data for Q1D model refinement. Additionally, a test projectile with a greater propellant mass fraction (10% or 20%) would allow any rocket effects to be more easily observed. Launching at lower speeds could also make the rocket's effect more observable. An alternate solid propellant is also suggested for successive design iterations, as black powder's structural integrity and combustion properties are not sufficiently consistent for simple modeling.

Though the results of these tests are not promising for a rocket augmented initial launch, further study is required before the technique can be conclusively rejected. Improved propellants and higher propellant mass ratio may provide the performance gains necessary to make this a viable launch technology.

REFERENCES

[1] A. Hertzberg, A. P. Bruckner, and D. W. Bogdanoff. "Ram Accelerator: A New Chemical Method for Accelerating Projectiles to Ultrahigh Velocities". In: *AIAA Journal* 26.2 (1988).

[2] C. Knowlen, A. P. Bruckner, D. W. Bogdanoff, and A. Hertzberg. "Performance Capabilities of the Ram Accelerator." In: *AIAA, ASME, SAE, ASEE 23rd Joint Propulsion Conference* (June 1987).

[3] A. P. Bruckner, C. Knowlen, A. Hertzberg, and D. W. Bogdanoff. "Operational Characteristics of the Thermally Choked Ram Accelerator". In: *Journal of Propulsion and Power* 7.2 (1991).

[4] D. L. Kruczynski, A. W. Horst, and T. C. Minor. *Experimental Demonstration of a 120-mm Ram Accelerator*. Tech. rep. ARL-TR-1237. Army Research Laboratory, Nov. 1996.

[5] A. Sasoh, S. Hirakata, Y. Ujigawa, and K. Takayama. "Operation Tests of a 25-mm bore ram accelerator". In: *Proceedings of AIAA, ASME, SAE, and ASEE Joint Propulsion Conference and Exhibit* (July 1996).

[6] C. Knowlen, A. J. Higgins, A. P. Bruckner, and P. Bauer. "Performance Capabilities of the Ram Accelerator." In: *AIAA, ASME, SAE, ASEE 23rd Joint Propulsion Conference* (June 1987).

[7] A. P. Bruckner. "The Ram Accelerator: A Technology Overview". In: *Proceedings of 40th Aerospace Sciences Meeting and Exhibit* AIAA 2002-1014 (Jan. 2002).

[8] A. J. Higgins, C. Knowlen, and A. P. Bruckner. "Ram Accelerator Operating Limits, Part 1: Identification of Limits". In: *Journal of Propulsion and Power*. 14.6 (Dec. 1998).

[9] A. J. Higgins, C. Knowlen, and A. P. Bruckner. "Ram Accelerator Operating Limits, Part 2: Nature of Observed Limits". In: *Journal of Propulsion and Power.* 14.6 (Dec. 1998).

[10] A. P. Bruckner and A. Hertzberg. "Ram Accelerator Direct Launch System for Space Cargo". In: *38th Congress of the International Astronautical Federation* (Oct. 1987).

[11] P. Kaloupis and A. P. Brucker. "The Ram Accelerator: A Chemically Driven Mass Launcher." In: *AIAA, ASME, SAE, ASEE 24th Joint Propulsion Conference* (July 1988).

[12] D. W. Bogdanoff. "Ram Accelerator Direct Space Launch System: New Concepts." In: *Journal of Propulsion and Power* 8.2 (Mar. 1992).

[13] D. Kruczynski, F. Liberatore, and M. Nusca. *An Analysis of Ram Acceleration for Specific Naval Applications.* Tech. rep. ARL-TR-1073. U.S. Army Research Laboratory, Apr. 1996.

[14] R. Witcofski, W. Scallion, Jr. D. Carter, and R. Courter. "An Advanced Hypervelocity Aerophysics Facility: A Ground-Based Flight-Test Range." In: *29th Aerospace Science Meeting* (Jan. 1991).

[15] A. P. Bruckner, C. Knowlen, and A. Hertzberg. "Applications of the Ram Accelerator to Hypervelocity Aerothermodynamic Testing." In: *AIAA 17th Aerospace Ground Testing Conference* (July 1992).

[16] Hypersciences Inc. *Risks and Disclosures.* 2018. URL: `https://www.sec.gov/Archives/edgar/data/1646921/000105291818000212/ex13-2.htm#_Toc515639075` (visited on 10/03/2018).

[17] E. Schultz. "The Subdetonative Ram Accelerator Starting Process". MA thesis. University of Washington, 1997.

[18] D. Kruczynski, C. Knowlen, C. Bundy, and A. P. Bruckner. "Low Velocity Start of Ram Accelerator: Obturator and Ignitor Effects". In: *35th AIAA, ASME, SAE, ASEE Joint Propulsion Conference and Exhibit.* AIAA 99-2265 (June 1999).

[19] C. Knowlen, E. Schultz, and A. P. Bruckner. "Investigation of Low Velocity Starting Techniques for the Ram Accelerator." In: *33rd Joint Propulsion Conference and Exhibit* (1997).

[20] C. Knowlen, J. F. Glusman, R. Grist, A. P. Bruckner, and A. J. Higgins. "Experimental Investigation of a Baffled-Tube Ram Accelerator." In: *52nd AIAA/SAE/ASEE Joint Propulsion Conference* (July 2016).

[21] C. Knowlen, T. Byrd, J. Dumas, N. Daneshvaran, J. Glusman, A. P. Bruckner, and A. J. Higgins. "Baffled-Tube Ram Accelerator OPeration with Inclined Baffles." In: *53rd AIAA/SAE/ASEE Joint Propulsion Conference* (July 2017).

[22] I. Ahmad. "The Problem of Gun Barrel Erosion: An Overview". In: *Gun Propulsion Technology.* Ed. by L. Stiefel. AIAA, 1988. Chap. 10, pp. 311–355.

[23] G. Bertrand, G. Gallagher, and J. J. Maroney. *A High Performance Experimental Smooth Bore Gun.* Tech. rep. D46-99-10-35. Canadian Armament Research and Development Establishment, July 1964.

[24] M. Giraud, J. F. Legendre, G. Simon, and L. Catoire. "Ram Accelerator in 90 mm Caliber: First Results Concerning the Scale Effect in the Thermally Choked Propulsion Mode." In: *13th International Symposium on Ballistics* (June 1992).

[25] C. Knowlen, C. Bundy, R. Schwab, and A. P. Bruckner. "University of Washington High Pressure Ram Accelerator Facility". In: *50th Meeting of the Aeroballistic Range Association* (Nov. 1999).

[26] P. G. Baer and I. W. May. "Traveling-Charge Effect". In: *Gun Propulsion Technology.* Ed. by L. Stiefel. AIAA, 1988. Chap. 15, pp. 499–536.

[27] R. E. Tompkins, K. J. White, W. F. Oberle, and A. A. Juhasz. *Traveling Charge Gun Firings Using Very High Burning Rate Propellants*. Tech. rep. BRL-TR-2970. US Army Ballistic Research Lab, Dec. 1988.

[28] B. S. Ermolaev, A. V. Romankov, A. A. Sulimov, and A. B. Crowley. "Compacted Modified Propellant Blocks as Traveling Charge in the Hybrid Shot Scheme". In: *Propellants Explos. Pyrotech.* 39.6 (2014).

[29] X. Lu, Y. Zhou, and Y. Yu. "Experimental and Numerical Investigations on Traveling Charge Gun Using Liquid Fuels". In: *Journal of Applied Mechanics* 78.5 (Sept. 2011).

[30] E. B. Fisher and S. Chandra. "A Dynamic Charging System for the Ram Accelerator for Hypervelocity Applications." In: *27th JANNAF Combustion Subcommittee Meeting* (Nov. 1990).

[31] J. Srulijes, G. Smeets, F. Seiler, A. George, G. Mathieu, and R. Resweber. "Shock Tube Validation Experiments for the Simulation of Ram-accelerator-related Combustion and Gasdynamic Problems". In: *Shock waves: Proceedings of the 18th International Symposium on Shock Waves*. June 1991.

[32] J. Srulijes, G. Smeets, and F. Seiler. "Expansion Tube Experiments for the Investigation of Ram-accelerator Combustion and Gasdynamic Problems". In: *AIAA, SAE, ASME, ASEE 28th Joint Propulsion Conference and Exhibit*. June 1992.

[33] A. Hertzberg, A. P. Bruckner, C. Knowlen, and K. A. McFall. "Method and Apparatus for Zero Velcoity Start Ram Acceleration". 5097743. 1992.

[34] K. McFall, C. Knowlen, A. P. Bruckner, and A. Hertzberg. "Numerical Analysis of Zero Velocity Start Technique for the Ram Accelerator." In: *32nd AIAA, ASME, SAE, and ASEE, Joint Propulsion Conference and Exhibit* (July 1996).

[35] J. L. Batson. *Rocket Exhaust Flow in Tube Launchers*. Tech. rep. RL-76-12. U.S. Army Missile Command, 1976.

[36] J. J. Bertin and J. L. Batson. "Experimentally Determined Rocket-Exhaust Flowfield in a Constrictive Tube Launcher". In: *Journal of Spacecraft and Rockets* 12.12 (1975).

[37] J. J. Bertin and J. L. Batson. "Comparison of Cold-Gas Simulations and Rocket-Launch Data for Constrictive Launchers". In: *Journal of Spacecraft and Rockets* 13.11 (Nov. 1976).

[38] H. H. Korst and J. J. Bertin. *The Analysis of Secondary Flows for Tube-Launched Rocket Configurations*. Tech. rep. TR-RL-CR-81-3. U.S. Army Missile Command, Jan. 1981.

[39] J. J. Bertin, R. S. Bertin, A. Yung, and G. Soohoo. "The Launch-Tube Flow-Field for a Vertical Launching System". In: *AIAA 26th Aerospace Sciences Meeting*. Jan. 1988.

[40] W. H. Miller and D. K. Barrington. "A Review of Contemporary Solid Rocket Motor Performance Prediction Techniques". In: *Journal of Spacecraft and Rockets* 7.3 (Mar. 1970).

[41] D. E. Coats, N. S. Cohen, J. N. Levine, and D. P. Karry III. *A Computer Program for the Prediction of Solid Propellant Rocket Motor Performance, Vol. I,II,III*. Tech. rep. AFRPL-TR-75-36. Air Force Rocket Propulsion Laboratory, 1975.

[42] B. K. Hodge and K. Koenig. "SOLROC, A Solid Rocket Motor Internal Ballistics Software Element". In: *30th AIAA, ASME, SAE, ASEE Joint Propulsion Conference*. AIAA-94-3115. AIAA, June 1994.

[43] A. Javed and D. Chakraborty. "Universal Erosive Burning Model Performance for Solid Rocket Motor Internal Ballistics". In: *Aerospace Science and Technology* 45.3 (Mar. 1970).

[44] F. Blomshield. "Lessons Learned In Solid Rocket Combustion Instability". In: *Missile Sciences Conference*. Nov. 2006.

[45] Y. Li, X. Chen, J. Xu, C. Zhou, and O. Musa. "Three-dimensional Multi-physics Coupled Simulation of Ignition Transient in a Dual Pulse Solid Rocket Motor". In: *Acta Astronautica* 146 (2018).

[46] L. d'Agostino and M. Andrenucci. "Unsteady Ballistic Code for Performance Prediction of Solid Propellant Rocket Engines". In: *43rd AIAA, ASME, SAE, ASEE Joint Propulsion Conference*. July 2007.

[47] T. Shimada, M. Hanzawa, T. Morita, T. Kato, T. Yoshikawa, and Y. Wada. "Stability Analysis of Solid Rocket Motor Combustion by Computational Fluid Dynamics". In: *AIAA Journal* 46.4 (Apr. 2008).

[48] V. Ferretti. "Numerical Simulations of Acoustic Resonance of Solid Rocket Motor". PhD thesis. University of Rome, 2009.

[49] E. Cavallini, V. Ferretti, B. Favini, M. Di Giacinto, and F. Serraglia. "Pressure Oscillations Numerical Simulation in Solid Rocket Motors". In: *48th Joint Propulsion Conference*. Aug. 2012.

[50] V. K. Chakravarthy, A. S. Iyer, and D. Chakraborty. "Quasi-One-Dimensional Modeling of Internal Ballistics and Axial Acoustics in Solid Rocket Motors". In: *Journal of Propulsion and Power* 32.4 (July 2016).

[51] S. Gordon and B. J. McBride. *Computer Program for Calculation of Complex Chemical Equilibrium Compositions and Applications*. Tech. rep. NASA Reference Publication 1311. NASA, 1996.

[52] J. D. Anderson. *Computational Fluid Dynamics: The Basics with Applications*. McGraw-Hill, 1995.

[53] A. Jameson, W. Schmidt, and E. Turkel. "Numerical Solution of the Euler Equations by Finite Volume Methods using Runge-Kutta Time-Stepping Schemes". In: *AIAA 14th Fluid and Plasma Dynamics Conference*. June 1981.

[54] G. A. Sod. “A Survey of Several Finite Difference Methods for Systems of Nonlinear Hyperbolic Conservation Laws.” In: *Journal of Computational Physics* 27.1 (1978).

[55] D. W. Bogdanoff, C. Knowlen, D. Murakami, and I. Stonich. “Magnetic Detector for Projectiles in Tubes”. In: *AIAA Journal* 28.11 (Nov. 1990).

Appendix A

ANALYTICAL MODELS

A.1 Model Assumptions

A.1.1 Geometry

The solid rocket motor and launch tube were modeled using a quasi-one-dimensional model. This model adapts the one-dimensional Euler equations for varying area. The system of equations is derived over the control volume depicted below in Fig. A.1. This formulation applies to the sections with and without propellant combustion. The burning rate is set to zero at stations where there is no propellant or the propellant is fully combusted. The computational domain was discretized into N control volumes with centers x_i, $i = 0, 1, 2, ..., N$.

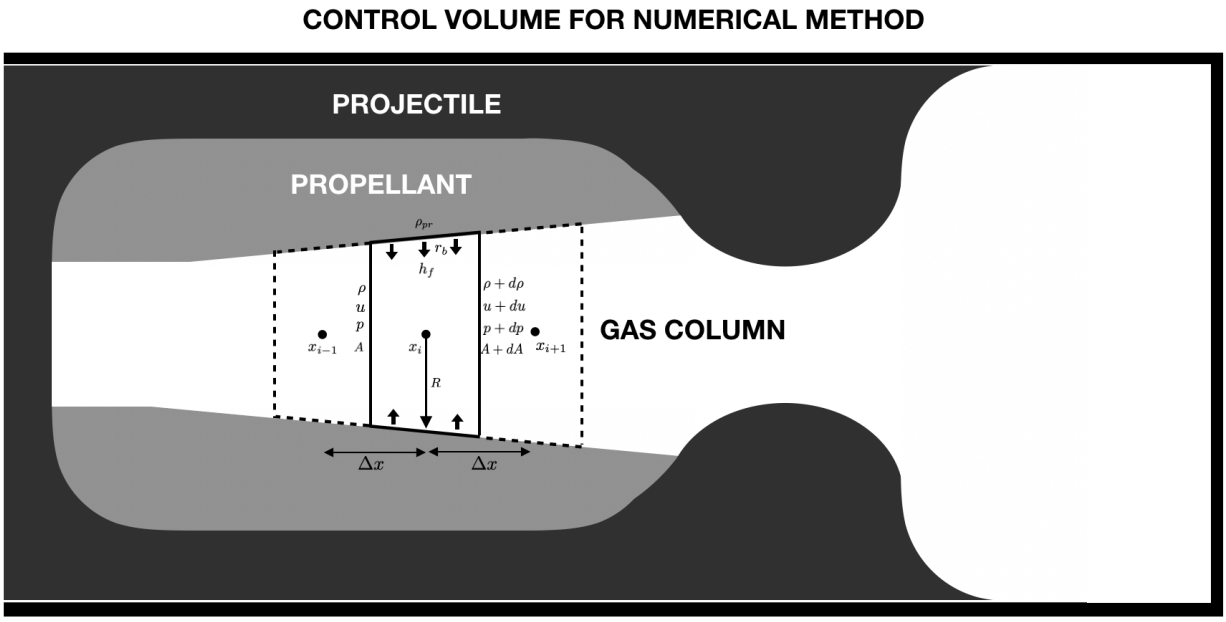

Figure A.1: Diagram of control volume for the quasi-one-dimensional model.

A.1.2 Physical Assumptions

Combustion of the propellant is assumed to occur in a thin planar region on the surface of the propellant charge. The combustion is assumed to be a function of pressure and governed by the De Vielle-Saint Robert law:

$$r_b = \beta\,(p)^n$$

where r_b is the linear burning rate and β and n are material properties determined empirically. Other burning rate laws have been investigated elsewhere in the literature for solid rocket motors and provide area for further modeling and study.

The gas in the chamber is assumed to follow the ideal gas law $p = \rho R_g T$. Additionally, the gas was assumed to be calorically perfect, so the specific internal energy could be calculated by $e = c_v T$. The combustion reaction was modeled in NASA CEA. The pressure and chemical composition were inputs, and the product properties and flame temperature, T_f, were outputs. From these the specific enthalpy of the products was computed, $h_f = c_p T_f$.

A.2 Developing the System of PDEs

A.2.1 Conservation of Mass:

The equation for conservation of mass over the control volume is

$$\frac{\partial}{\partial t}\iiint_V (\rho\, d\forall) + \iint_S \rho\mathbf{u}\cdot\mathbf{dS} = 0.$$

The first term becomes

$$\frac{\partial}{\partial t}\iiint_V (\rho\, d\forall) = \frac{\partial}{\partial t}\left(\rho A\, dx\right).$$

The second term becomes

$$\iint_S \rho\mathbf{u}\cdot\mathbf{dS} = -\rho u A + (\rho + d\rho)\,(u + du)\,(A + dA) - A_b r_b \rho_{pr}$$

which multiplied out yields

$$\iint_S \rho\mathbf{u}\cdot\mathbf{dS} = -\rho uA + \rho uA + \rho u\, dA + \rho A\, du + d\rho\, uA + \rho\, du\, dA + V\, d\rho\, dA + A\, d\rho\, du + d\rho\, dA\, du - A_b r_b \rho_{pr}$$

where A_b is the area of burning propellant, r_b is the linear burning rate, and ρ_{pr} is the propellant density. As dx becomes small, the terms with products of differentials go to zero. Eliminating these terms and simplifying gives

$$\begin{aligned}\iint_S \rho\mathbf{u}\cdot\mathbf{dS} &= \rho u\,dA + \rho A\,du + d\rho\,uA - A_b r_b \rho_{pr} \\ &= d\left(\rho u A\right) - A_b r_b \rho_{pr}.\end{aligned}$$

Substituting into the original conservation of mass equation yields

$$\frac{\partial}{\partial t}\left(\rho A\,dx\right) + d\left(\rho u A\right) = A_b r_b \rho_{pr}.$$

Then dividing by dx yields

$$\frac{\partial}{\partial t}\left(\rho A\right) + d\left(\rho u A\right)/dx = A_b r_b \rho_{pr}/dx.$$

Note that the A_b/dx is P_b, the perimeter of the burning area. Also, $d\left(\rho u A\right)/dx$ becomes $\partial\left(\rho u A\right)/\partial x$, yielding

$$\frac{\partial\left(\rho A\right)}{\partial t} + \frac{\partial\left(\rho u A\right)}{\partial x} = P_b r_b \rho_{pr}.$$

A.2.2 Conservation of Momentum:

The equation for conservation of momentum over the control volume is

$$\frac{\partial}{\partial t}\iiint_V \left(\rho u\,dV\right) + \iint_S \left(\rho u\mathbf{u}\right)\cdot\mathbf{dS} = -\iint_S \left(p\,dS\right)_x.$$

The first term becomes

$$\frac{\partial}{\partial t}\iiint_V \left(\rho u\,dV\right) = \frac{\partial}{\partial t}\left(\rho u A\,dx\right).$$

The second term becomes

$$\iint_S \left(\rho u\mathbf{u}\right)\cdot\mathbf{dS} = -\rho u^2 A + \left(\rho + d\rho\right)\left(u + du\right)^2\left(A + dA\right)$$

which multiplied out yields

$$\iint_S (\rho u \mathbf{u}) \cdot \mathbf{dS} = -\rho u^2 A + \rho u^2 A + 2\rho u A\, du + \rho A\, du^2 + \rho u^2\, dA + 2\rho u\, du\, dA + \rho\, du^2\, dA$$
$$+ u^2 A\, d\rho + 2uA\, d\rho\, du + A\, d\rho\, du^2 + u^2\, dA\, d\rho + 2u\, du\, dA\, d\rho + d\rho\, du^2\, dA.$$

Eliminating the terms with products of differentials and simplifying

$$\iint_S \rho \mathbf{u} \cdot \mathbf{dS} = 2\rho u A\, du + \rho u^2\, dA + u^2 A\, d\rho$$
$$= d\left(\rho u^2 A\right).$$

The term on the right side becomes

$$\iint_S (p\, dS)_x = -pA + (p + dp)(A + dA) - p\, dA$$
$$= -A\, dp$$

Substituting into the original conservation of momentum equation yields

$$\frac{\partial}{\partial t}(\rho u A\, dx) + d\left(\rho u^2 A\right) = -A\, dp.$$

Then dividing by dx yields

$$\frac{\partial}{\partial t}(\rho u A) + d\left(\rho u^2 A\right)/dx = -A\, dp/dx.$$

Note that $d\left(\rho u^2 A\right)/dx$ becomes $\partial\left(\rho u^2 A\right)/\partial x$ and dp/dx becomes $\partial p/\partial x$, yielding

$$\frac{\partial(\rho u A)}{\partial t} + \frac{\partial\left(\rho u^2 A\right)}{\partial x} = -A\frac{\partial p}{\partial x}.$$

Adding $\frac{\partial(puA)}{\partial x} = A\frac{\partial p}{\partial x} + p\frac{\partial A}{\partial x}$ to each side

$$\frac{\partial(\rho u A)}{\partial t} + \frac{\partial\left[\left(\rho u^2 + p\right) A\right]}{\partial x} = p\frac{\partial A}{\partial x}.$$

A.2.3 Conservation of Energy:

The equation for conservation of energy over the control volume is

$$\frac{\partial}{\partial t}\iiint_V \rho\left(e+\frac{u^2}{2}\right)\,dV+\iint_S \rho\left(e+\frac{u^2}{2}\right)\mathbf{u}\cdot\mathbf{dS}=-\iint_S (p\mathbf{u})\cdot\mathbf{dS}.$$

The first term becomes

$$\frac{\partial}{\partial t}\iiint_V \rho\left(e+\frac{u^2}{2}\right)\,dV=\frac{\partial}{\partial t}\left(\rho\left(e+\frac{u^2}{2}\right)A\,dx\right).$$

The second term becomes

$$\begin{aligned}\iint_S \rho\left(e+\frac{u^2}{2}\right)\mathbf{u}\cdot\mathbf{dS}=&-\rho\left(e+\frac{u^2}{2}\right)uA+(\rho+d\rho)\left(e+de+\frac{(u+du)^2}{2}\right)(u+du)\,(A+dA)\\&-r_bA_b\rho_{pr}h_f\end{aligned}$$

where h_f is the specific reaction enthalpy of the combustion, which multiplied out yields

$$\begin{aligned}\iint_S \rho\left(e+\frac{u^2}{2}\right)\mathbf{u}\cdot\mathbf{dS}=&\,dA\,de\,d\rho\,du+A\,de\,d\rho\,du+\frac{1}{2}A\,d\rho\,du^3+\frac{1}{2}dA\,d\rho\,du^3+Ae\,d\rho\,du+e\,dA\,d\rho\,du\\&+A\,de\,du\,\rho+dA\,de\,du\,\rho+\frac{1}{2}A\,du^3\,\rho+\frac{1}{2}dA\,du^3\,\rho+A\,du\,e\rho+dA\,du\,e\rho\\&+A\,de\,d\rho\,u+dA\,de\,d\rho\,u+\frac{3}{2}A\,d\rho\,du^2\,u+\frac{3}{2}dA\,d\rho\,du^2\,u+A\,d\rho\,eu+dA\,d\rho\,eu\\&+A\,de\,\rho u+dA\,de\,\rho u+\frac{3}{2}A\,du^2\,\rho u+\frac{3}{2}\,dA\,du^2\rho u+dA\,e\rho u+\frac{3}{2}A\,d\rho duu^2\\&+\frac{3}{2}dA\,d\rho\,du\,u^2+\frac{3}{2}A\,du\,\rho u^2+\frac{3}{2}dA\,du\,\rho u^2+\frac{1}{2}A\,d\rho\,u^3+\frac{1}{2}dA\,d\rho\,u^3+\frac{1}{2}dA\,\rho u^3\\&-r_bA_b\rho_{pr}h_f\end{aligned}$$

As dx becomes small, the terms with products of differentials go to zero. Eliminating these terms and simplifying gives

$$\begin{aligned}\iint_S \rho\left(e+\frac{u^2}{2}\right)\mathbf{u}\cdot\mathbf{dS}=&\,A\,du\,e\rho+A\,d\rho\,eu+A\,de\,\rho u+dA\,e\rho u\\&+\frac{3}{2}A\,du\,\rho u^2+\frac{1}{2}A\,d\rho\,u^3+\frac{1}{2}dA\,\rho u^3-r_bA_b\rho_{pr}h_f\\=&\,d\left(\rho uA\left(e+\frac{u^2}{2}\right)\right)-r_bA_b\rho_{pr}h_f\end{aligned}$$

The term on the right hand side becomes

$$\begin{aligned} -\iint_S (p\mathbf{u}) \cdot \mathbf{dS} &= -\left[-puA + (p+dp)(u+du)(A+dA)\right] \\ &= -d(puA) \end{aligned}$$

Substituting into the original conservation of mass equation yields

$$\frac{\partial}{\partial t}\left(\rho\left(e+\frac{u^2}{2}\right)A\,dx\right) + d\left(\rho uA\left(e+\frac{u^2}{2}\right)\right) = -d(puA) + r_b A_b \rho_{pr} h_f.$$

Then dividing by dx yields

$$\frac{\partial}{\partial t}\left(\rho\left(e+\frac{u^2}{2}\right)A\right) + \frac{\partial}{\partial x}\left(\rho uA\left(e+\frac{u^2}{2}+p/\rho\right)\right) = r_b P_b \rho_{pr} h_f.$$

A.2.4 System of PDEs

The the full set of PDEs for this system:

$$\begin{aligned} \frac{\partial(\rho A)}{\partial t} + \frac{\partial(\rho uA)}{\partial x} &= P_b r_b \rho_{pr} \\ \frac{\partial(\rho uA)}{\partial t} + \frac{\partial\left[(\rho u^2 + p)A\right]}{\partial x} &= p\frac{\partial A}{\partial x} \\ \frac{\partial}{\partial t}\left(\rho\left(e+\frac{u^2}{2}\right)A\right) + \frac{\partial}{\partial x}\left(\rho uA\left(e+\frac{u^2}{2}+p/\rho\right)\right) &= r_b P_b \rho_{pr} h_f. \end{aligned}$$

This system can be rewritten as

$$\frac{\partial \mathbf{U}}{\partial t} + \frac{\partial \mathbf{F}}{\partial x} = \mathbf{J} + p\frac{\partial \mathbf{A}}{\partial x}$$

where

$$\mathbf{U} = \begin{pmatrix} \rho A \\ \rho uA \\ \rho\left(e+\frac{u^2}{2}\right)A \end{pmatrix}, \mathbf{F} = \begin{pmatrix} \rho uA \\ (\rho u^2 + p)A \\ \rho uA\left(e+\frac{u^2}{2}+\frac{p}{\rho}\right) \end{pmatrix}, \mathbf{J} = \begin{pmatrix} P_b r_b \rho_{pr} \\ 0 \\ r_b P_b \rho_{pr} h_f \end{pmatrix}, \mathbf{A} = \begin{pmatrix} 0 \\ A \\ 0 \end{pmatrix}.$$

A.3 Numerical Methods

A.3.1 MacCormack Scheme

After applying the constitutive equations we get the system in the form of

$$\frac{\partial \mathbf{U}}{\partial t} + \frac{\partial \mathbf{F}}{\partial x} = \mathbf{J} + p\frac{\partial \mathbf{A}}{\partial x}$$

or

$$\frac{\partial \mathbf{U}}{\partial t} = \mathbf{J} - \frac{\partial \mathbf{F}}{\partial x} + p\frac{\partial \mathbf{A}}{\partial x}.$$

The space is discretized into cells centered at $x_1, x_2, ..., x_N$. The properties at x_i are denoted by the subscript i. The distance $x_i - x_{i-1}$ is denoted as Δx. The timesteps are denoted by the superscript t or $t + \Delta t$. A second order MacCormack method is used.

Predictor step:

$$\left(\frac{\partial \mathbf{U}}{\partial t}\right)_i^t = \mathbf{J}_i^t - \left(\frac{\mathbf{F}_{i+1}^t - \mathbf{F}_i^t}{\Delta x}\right) + p_i^t \left(\frac{\mathbf{A}_{i+1}^t - \mathbf{A}_i^t}{\Delta x}\right). \tag{A.1}$$

$$\overline{\mathbf{U}}_i^{t+\Delta t} = \mathbf{U}_i^t + \left(\frac{\partial \mathbf{U}}{\partial t}\right)_i^t \Delta t$$

From $\overline{\mathbf{U}}_i^{t+\Delta t}$, we calculate $\overline{p}_i^{t+\Delta t}$, $\overline{\mathbf{J}}_i^{t+\Delta t}$, and $\overline{\mathbf{F}}_i^{t+\Delta t}$. A similar approach is used for the area change in the sections with propellant burning. The area of the section is $A = \pi R^2$, the time derivative of this is

$$\frac{\partial A}{\partial t} = 2\pi R\frac{dR}{dt} = 2\pi R r_b = 2r_b\sqrt{\pi A} = 2\beta\left(p\right)^n\sqrt{\pi A}$$

or

$$\left(\frac{\partial A}{\partial t}\right)_i^t = 2\beta\left(p_i^t\right)^n\sqrt{\pi A_i^t}$$

Thus we can find $\overline{A}_i^{t+\Delta t}$ and also $\overline{\mathbf{A}}_i^{t+\Delta t}$:

$$\overline{A}_i^{t+\Delta t} = A_i^t + \left(\frac{\partial A}{\partial t}\right)_i^t \Delta t$$

Corrector step:

$$\left(\overline{\frac{\partial \mathbf{U}}{\partial t}}\right)_i^{t+\Delta t} = \overline{\mathbf{J}}_i^{t+\Delta t} - \left(\frac{\overline{\mathbf{F}}_i^{t+\Delta t} - \overline{\mathbf{F}}_{i-1}^{t+\Delta t}}{\Delta x}\right) + \overline{p}_i^{t+\Delta t}\left(\frac{\overline{\mathbf{A}}_i^{t+\Delta t} - \overline{\mathbf{A}}_{i-1}^{t+\Delta t}}{\Delta x}\right) \tag{A.2}$$

$$\left(\frac{\partial \mathbf{U}}{\partial t}\right)_{avg} = \frac{1}{2}\left[\left(\frac{\partial \mathbf{U}}{\partial t}\right)_i^t + \left(\overline{\frac{\partial \mathbf{U}}{\partial t}}\right)_i^{t+\Delta t}\right]$$

$$\mathbf{U}_i^{t+\Delta t} = \mathbf{U}_i^t + \left(\frac{\partial \mathbf{U}}{\partial t}\right)_{avg}\Delta t \tag{A.3}$$

The corrector step was applied to the area change:

$$\left(\overline{\frac{\partial A}{\partial t}}\right)_i^{t+\Delta t} = 2\beta\left(\overline{p}_i^{t+\Delta t}\right)^n\sqrt{\pi\overline{A}_i^{t+\Delta t}}$$

$$\left(\overline{\frac{\partial A}{\partial t}}\right)_{avg} = \frac{1}{2}\left[\left(\frac{\partial A}{\partial t}\right)_i^t + \left(\frac{\partial A}{\partial t}\right)_i^{t+\Delta t}\right]$$

$$A_i^{t+\Delta t} = A_i^t + \left(\frac{\partial A}{\partial t}\right)_{avg}\Delta t$$

Note the forward differencing in the predictor step (Eqn. A.1) and backward differencing in the corrector step (Eqn. A.2). This scheme can be reversed to backward differencing in the predictor and forward in the corrector. To prevent biasing the differencing direction was alternated each timestep.

A.3.2 Numerical Viscosity

Additional stability is added to the method by adding a numerical viscosity term $\mathbf{D}$ in the equation for $\mathbf{U}_i^{t+\Delta t}$. The viscosity formulation used here is explained in detail by Jameson et al. [53]. A summary of the method is included here. For each cell a parameter ν_i is calculated. The parameters $\kappa^{(2)}$ and $\kappa^{(4)}$ define the respective second- and fourth-order diffusion rates. Note that all quantities in this calculation are in the current timestep, t, unless otherwise designated. The superscript t has been omitted for simplicity.

$$\nu_i = \frac{|p_{i+1} - 2p_i + p_{i-1}|}{|p_{i+1}| - 2|p_i| + |p_{i-1}|}$$

The parameters $\epsilon^{(2)}$ and $\epsilon^{(4)}$ are calculated for the left and right sides of each cell:

$$\epsilon^{(2)}_{R,i} = \kappa^{(2)} \max(\nu_{i+1}, \nu_i)$$
$$\epsilon^{(2)}_{L,i} = \kappa^{(2)} \max(\nu_i, \nu_{i-1})$$

and

$$\epsilon^{(4)}_{R,i} = \max\left(0, \left(\kappa^{(4)} - \epsilon^{(2)}_{R,i}\right)\right)$$
$$\epsilon^{(4)}_{L,i} = \max\left(0, \left(\kappa^{(4)} - \epsilon^{(2)}_{L,i}\right)\right).$$

The the terms $\mathbf{d}_L$, $\mathbf{d}_R$, and $\mathbf{D}$ were calculated:

$$\mathbf{d}_{R,i} = \epsilon^{(2)}_{R,i}(\mathbf{U}_{i+1} - \mathbf{U}_i) - \epsilon^{(4)}_{R,i}(\mathbf{U}_{i+2} - 3\mathbf{U}_{i+1} + 3\mathbf{U}_i - \mathbf{U}_{i-1})$$
$$\mathbf{d}_{L,i} = \epsilon^{(2)}_{L,i}(\mathbf{U}_i - \mathbf{U}_{i-1}) - \epsilon^{(4)}_{L,i}(\mathbf{U}_{i+1} - 3\mathbf{U}_i + 3\mathbf{U}_{i-1} - \mathbf{U}_{i-2})$$
$$\mathbf{D}_i = \mathbf{d}_{R,i} - \mathbf{d}_{L,i}.$$

This $\mathbf{D}_i$ vector was added to the solution vector on the iteration step. So Equation A.3 becomes

$$\mathbf{U}_i^{t+\Delta t} = \mathbf{U}_i^t + \left(\frac{\partial \mathbf{U}}{\partial t}\right)_{avg} \Delta t + \mathbf{D}_i.$$

A.3.3 Determining Timestep

The timestep Δt is defined by

$$(\Delta t)_i^t = C\frac{\Delta x}{a_i^t + |u_i^t|}$$

where C is the CFL number and $a_i^t = \sqrt{\gamma_i^t R_{g,i}^t T_i^t}$ is the local sound speed. Because this formula results in different timesteps across the domain, the minimum $(\Delta t)_i$ is used in each step:

$$(\Delta t)^t = \min\left[(\Delta t)_1^t, (\Delta t)_2^t, ..., (\Delta t)_N^t\right].$$

A.3.4 Boundary Conditions

Boundary conditions were enforced on the model with boundary cells, which were linearly interpolated from the last two existing cells and had axial velocity, u, set to zero. In Eqn. A.1 for example, for the last cell $i = N$, the $\mathbf{F}_{N+1}^t$ term was set to

$$\mathbf{F}_{N+1}^t = \begin{pmatrix} 0 \\ p_{N+1}^t A_{N+1}^t \\ 0 \end{pmatrix}$$

where $p_{N+1}^t = 2p_N^t - p_{N-1}^t$ and $A_{N+1}^t = 2A_N^t - A_{N-1}^t$.

A.3.5 Gas Properties

The gas properties are defined in each cell by $\gamma_i^t, c_{v,i}^t, c_{p,i}^t$ where $\gamma = c_p/c_v$. In general, for a mixture of gases with masses m_1 and m_2, the specific heat is

$$c_v = \frac{m_1 c_{v,1} + m_2 c_{v,2}}{m_1 + m_2}.$$

To find the specific heats at the next timestep, we add

$$c_{v,i}^{t+\Delta t} = \frac{\left(\rho_i^t A_i^t \Delta x\right) c_{v,i}^t + \left(\rho_{i-\frac{1}{2}} A_{i-\frac{1}{2}} u_{i-\frac{1}{2}} \Delta t\right) c_{v,i-1}^t - \left(\rho_{i+\frac{1}{2}} A_{i+\frac{1}{2}} u_{i+\frac{1}{2}} \Delta t\right) c_{v,i}^t + \left(\rho_{pr} r_b P_b \Delta x \Delta t\right) c_{v,prod}}{\left(\rho_i^t A_i^t \Delta x\right) + \left(\rho_{i-\frac{1}{2}} A_{i-\frac{1}{2}} u_{i-\frac{1}{2}} \Delta t\right) - \left(\rho_{i+\frac{1}{2}} A_{i+\frac{1}{2}} u_{i+\frac{1}{2}} \Delta t\right) + \left(\rho_{pr} r_b P_b \Delta x \Delta t\right)}$$

where $A_{i-1/2} = \frac{1}{2}\left(A_{i-1} + A_i\right), A_{i+1/2} = \frac{1}{2}\left(A_i + A_{i+1}\right)$ and the remaining quantities are calculated:

$$\begin{aligned}
\rho_i &= \frac{1}{2}\left(\rho_i^t + \overline{\rho}_i^{t+\Delta t}\right) \\
u_i &= \frac{1}{2}\left(u_i^t + \overline{u}_i^{t+\Delta t}\right) \\
\rho_{i-\frac{1}{2}} &= \frac{\rho_{i-1} + \rho_i}{2}, \ \rho_{i+\frac{1}{2}} = \frac{\rho_i + \rho_{i+1}}{2} \\
u_{i-\frac{1}{2}} &= \frac{u_{i-1} + u_i}{2}, \ u_{i+\frac{1}{2}} = \frac{u_i + u_{i+1}}{2} \\
r_b &= \beta\left(p_i\right)^n .
\end{aligned}$$

This procedure is repeated for $c_{p,i}^{t+\Delta t}$ and then the ratio of specific heats is calculated:

$$\gamma_i^{t+\Delta t} = \frac{c_{p,i}^{t+\Delta t}}{c_{v,i}^{t+\Delta t}}$$

and the gas constant, R_g, is calculated:

$$R_{g,i}^{t+\Delta t} = c_{p,i}^{t+\Delta t} - c_{v,i}^{t+\Delta t}.$$

.

Appendix B

TEST ARTICLE DRAWINGS

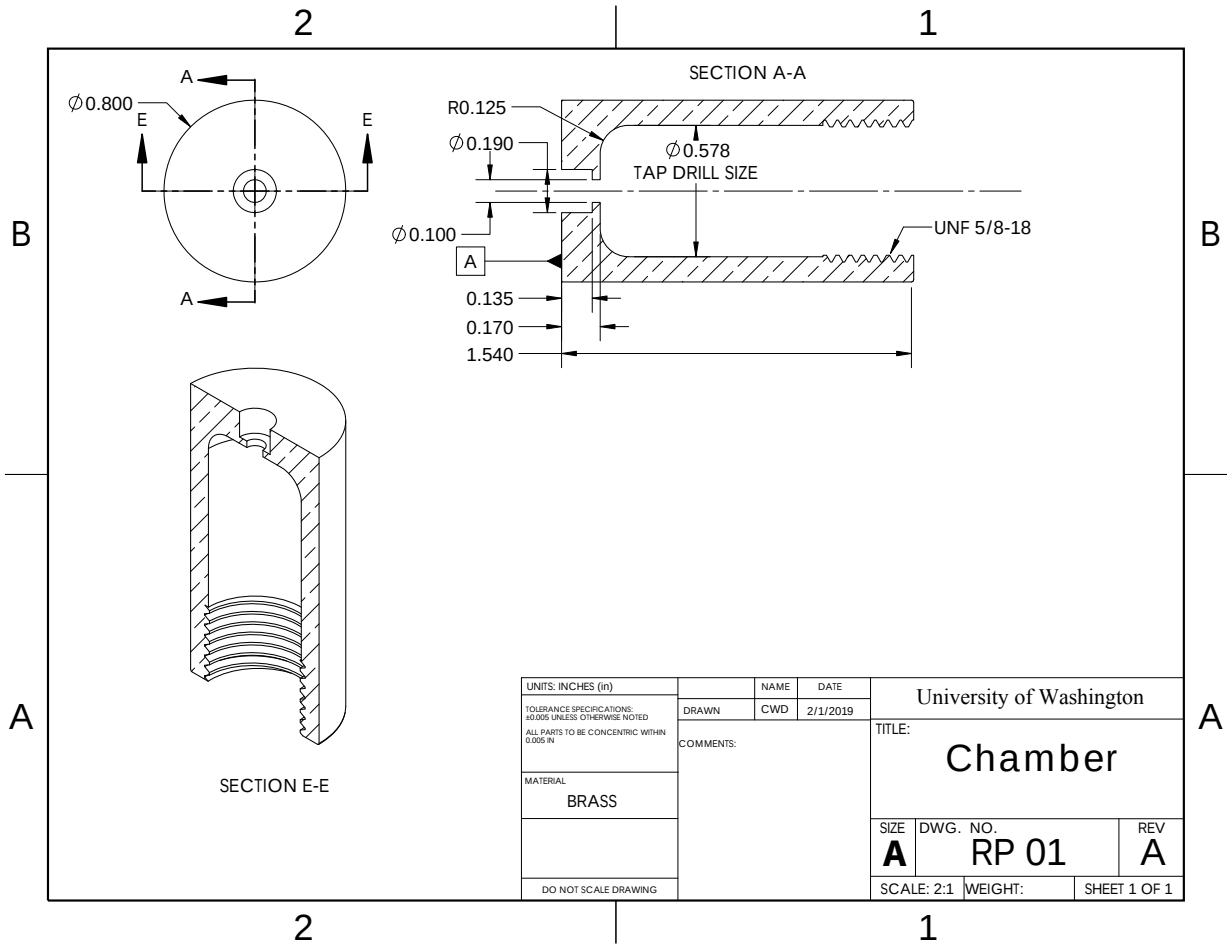

Figure B.1: Full projectile.

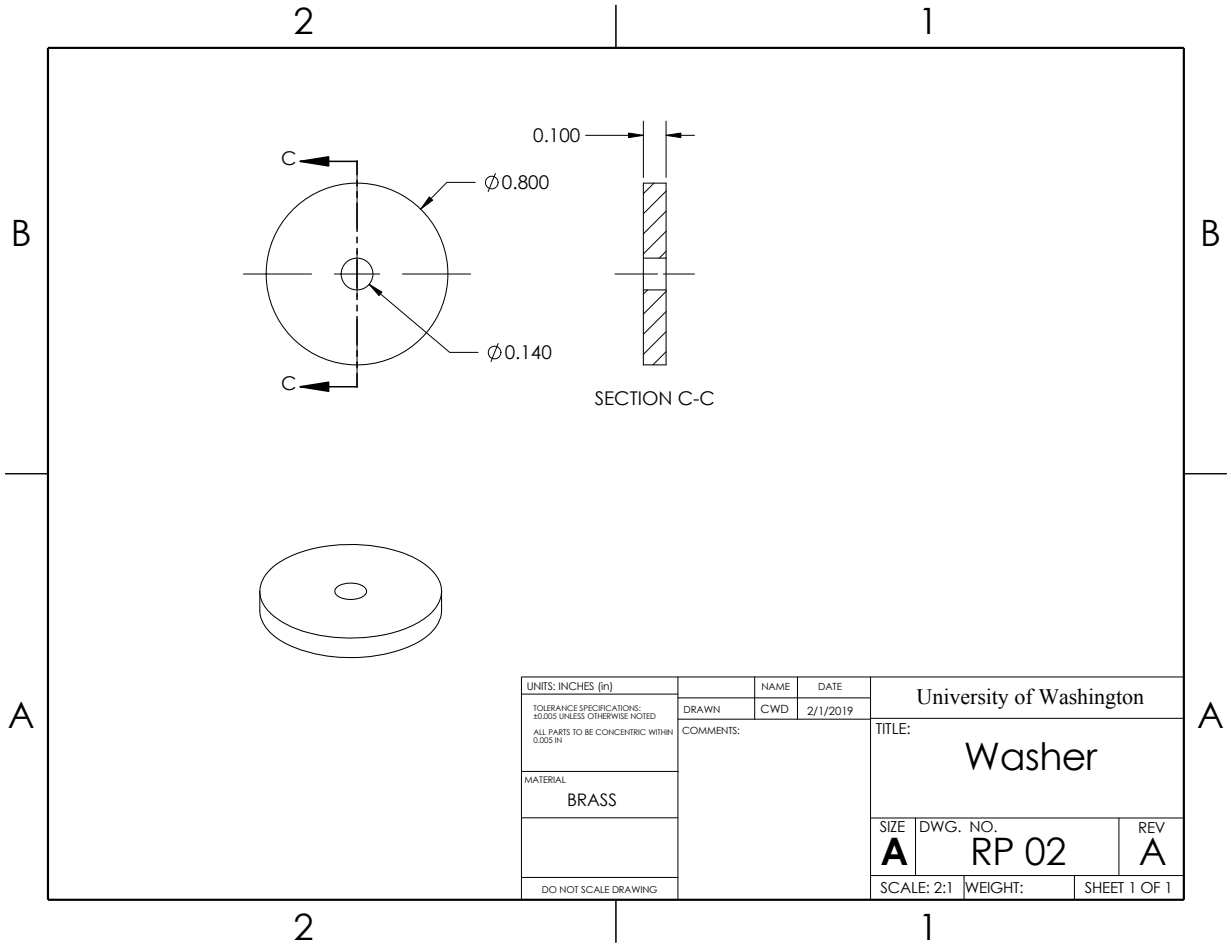

Figure B.2: Combustion chamber.

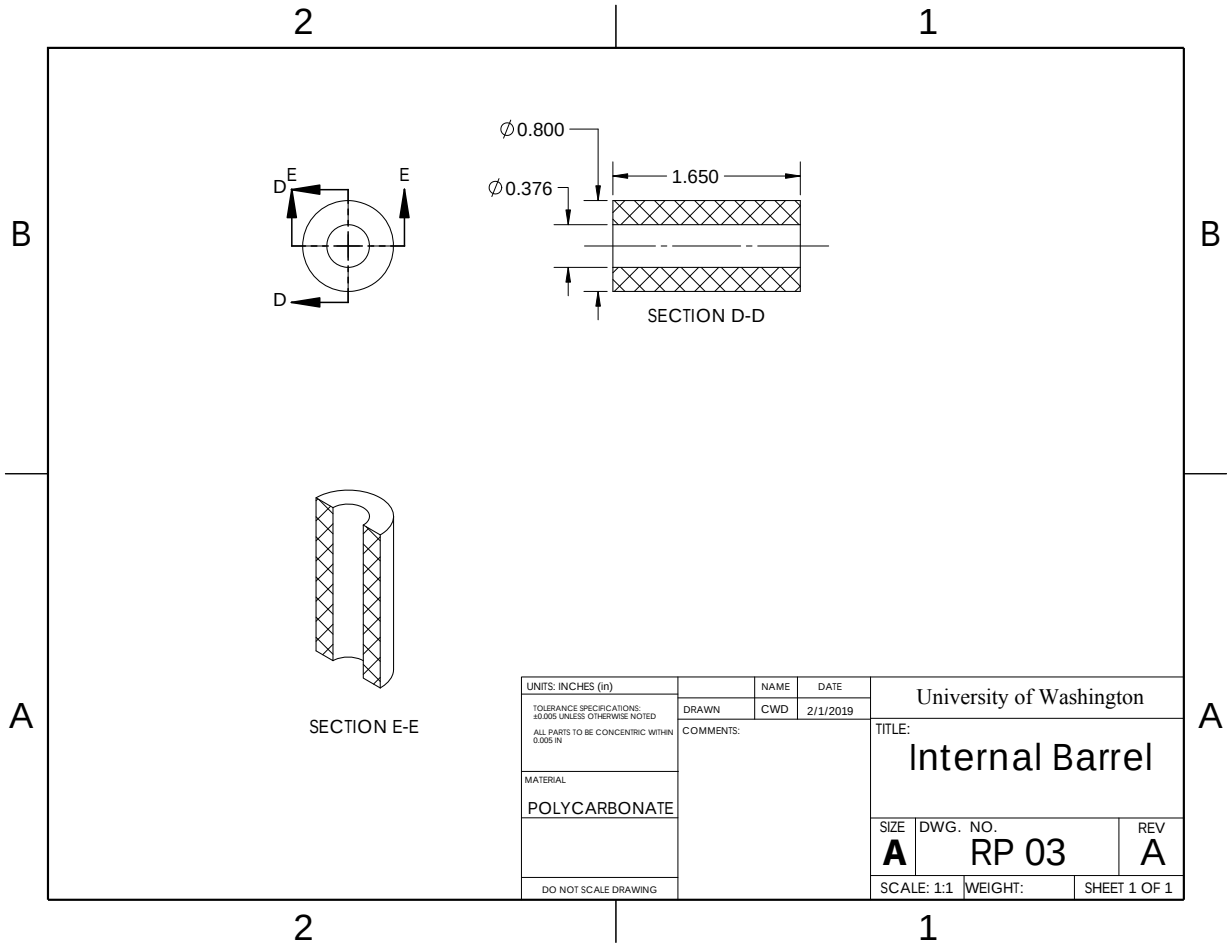

Figure B.3: Combustion chamber cap.

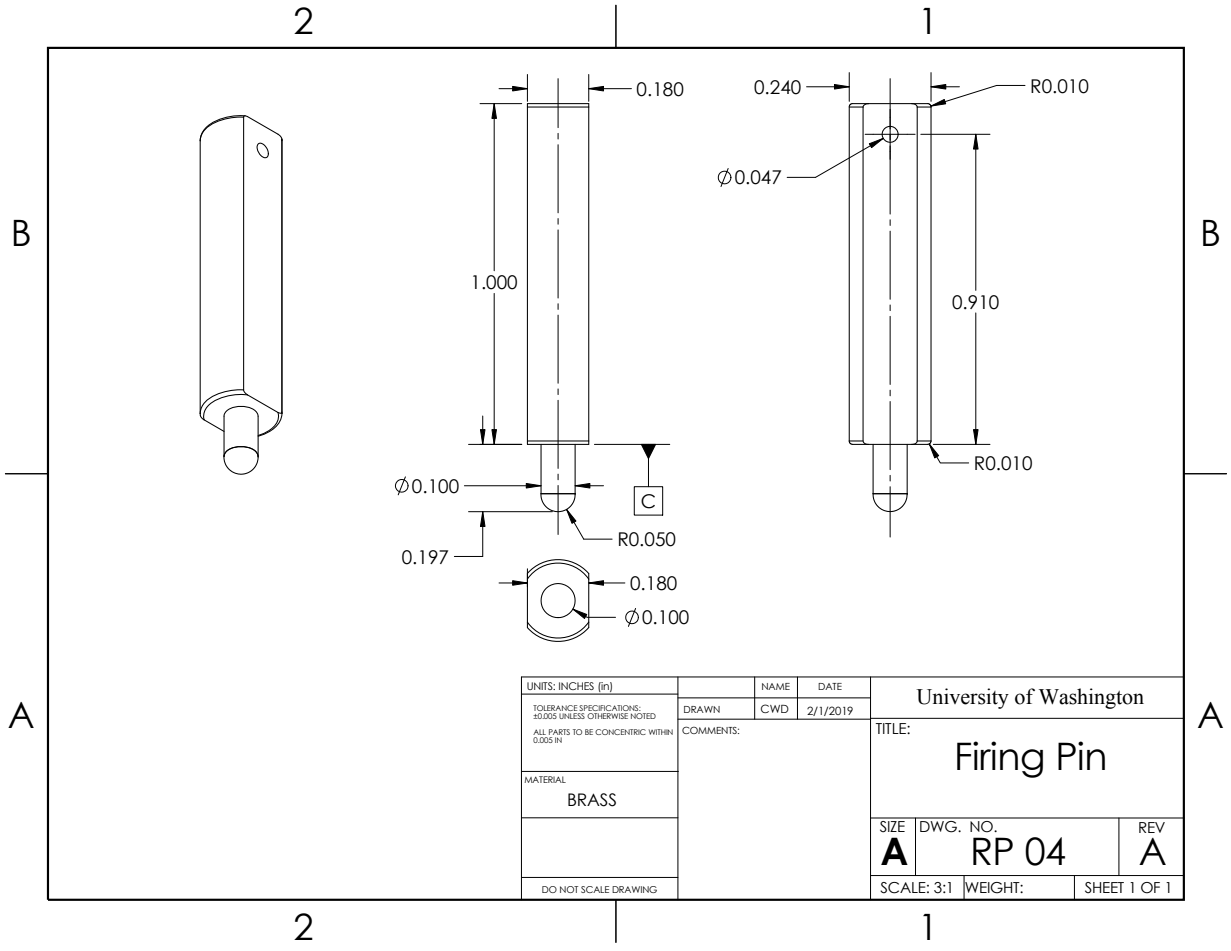

Figure B.4: External projectile housing.

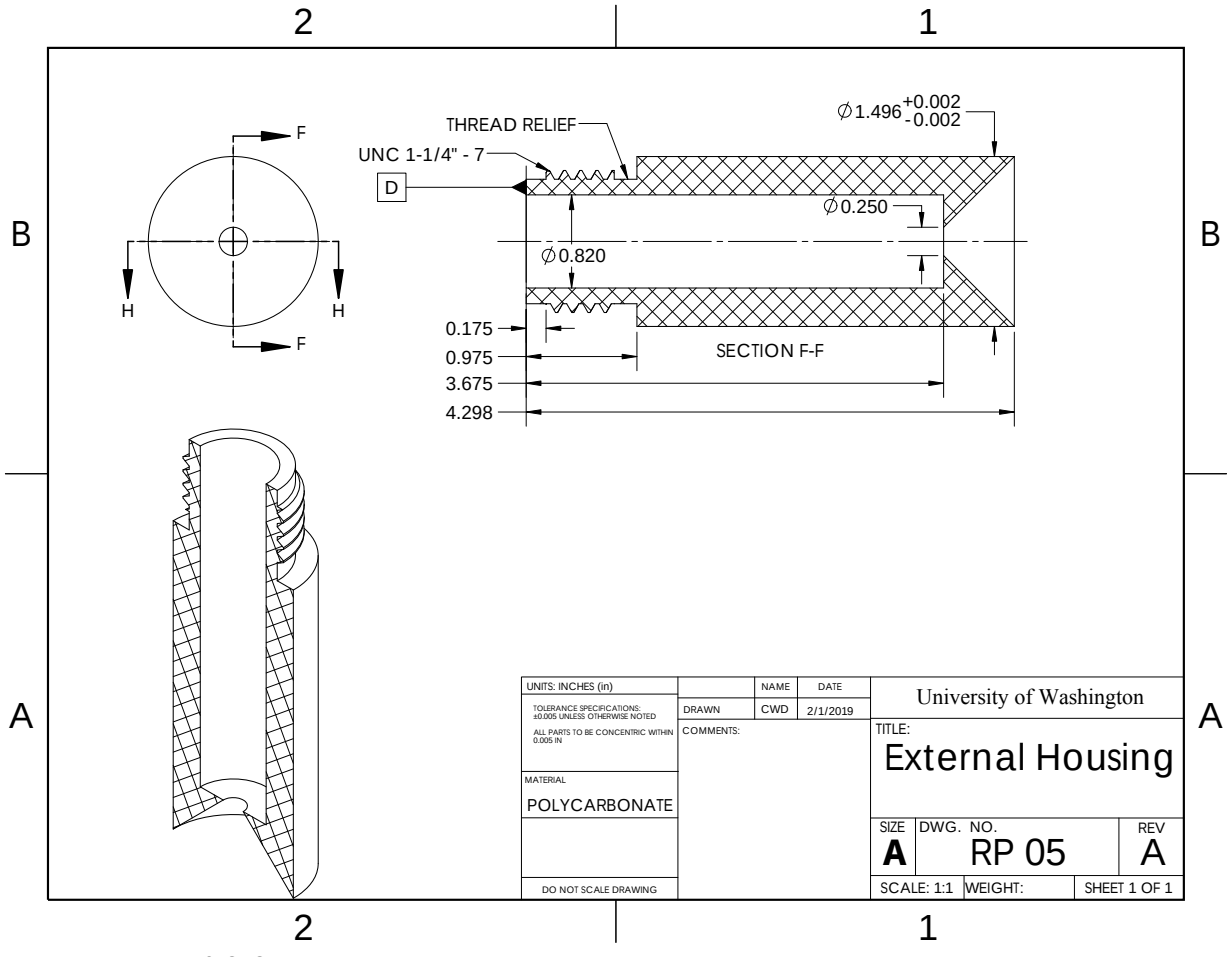

Figure B.5: Internal barrel and firing pin.

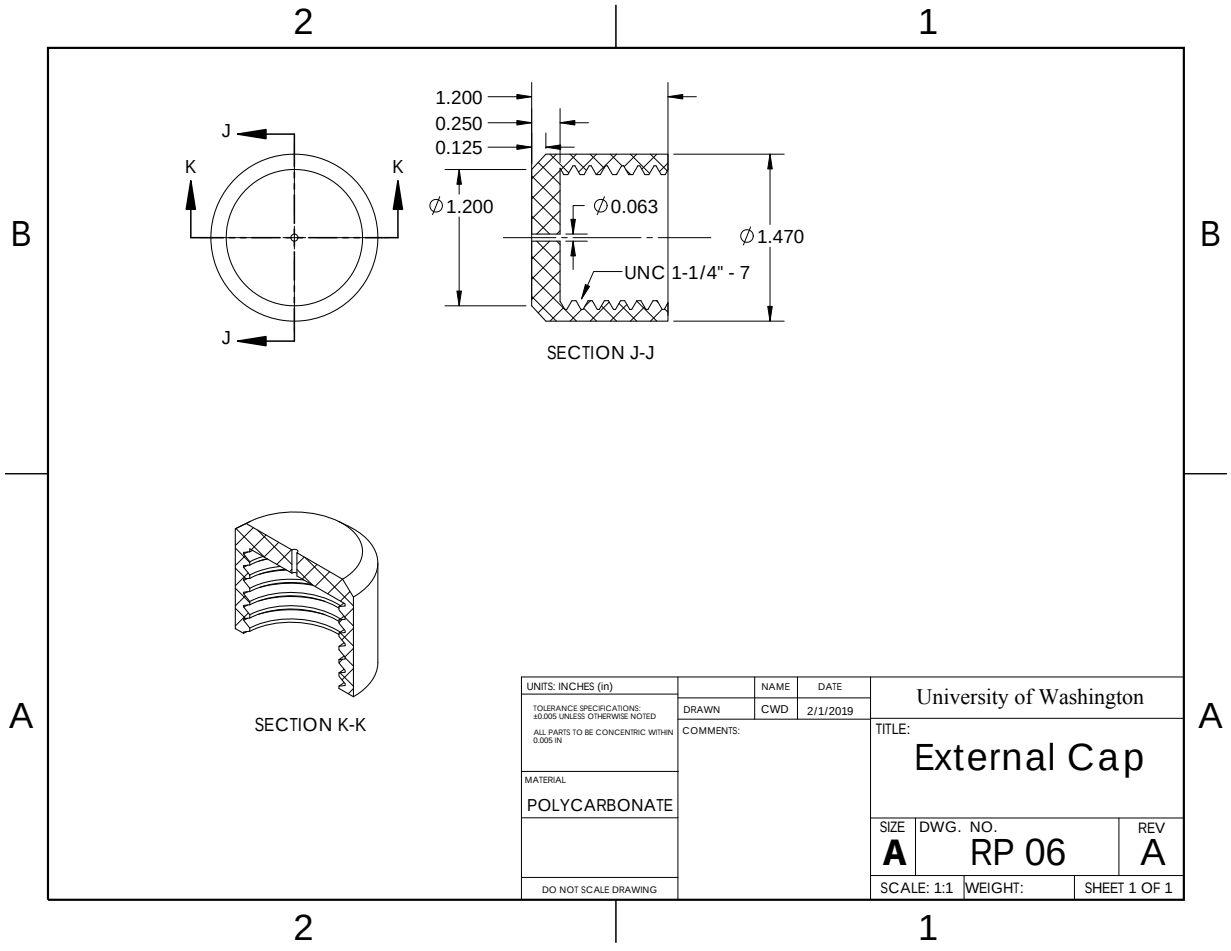

Figure B.6: External projectile housing.

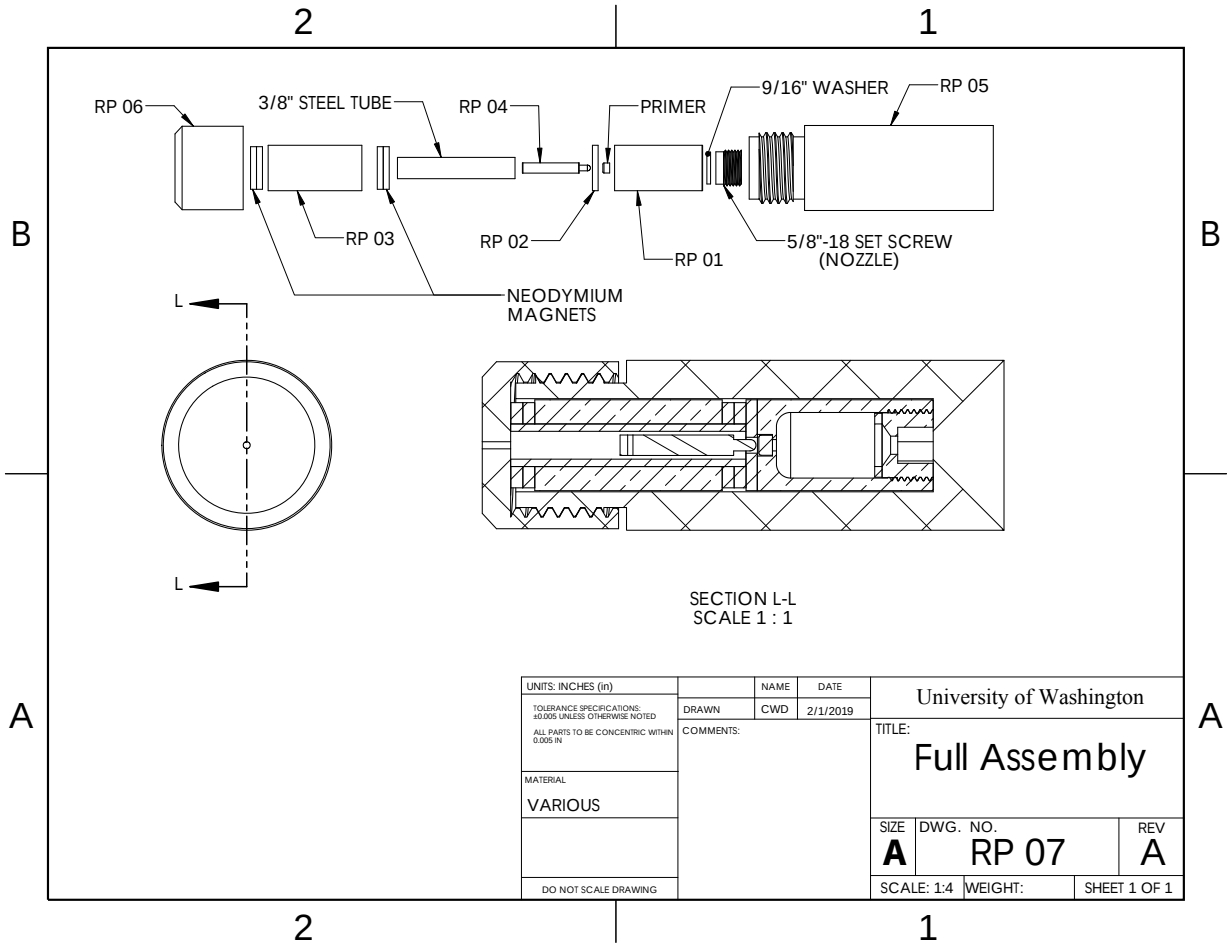

Figure B.7: Internal barrel and firing pin.

Appendix C

MATLAB CODE

C.1 MATLAB Code - Main.m

```
%Main.m - Primary executable script for Q1D simulation of in-tube rocket
% This program uses a MacCormack scheme with second and fourth order
% artificial viscosity to solve a Q1D model of a projectile with an onboard
% rocket. This program is intended to provide an estimate of the chamber
% pressure and projectile acceleration, velocity, and position profiles.
%
% Other m-files required: geometry.m,flameTemp.m
%
%
% Author: Clayton Davis
%
% email: daviscw@uw.edu
%
% Jan 2019; Last revision: 8-Feb-2019
%% Initial Conditions
clear all
close all

%save material parameters of nitrogen
cp_N2 = 1040; %J/(kg K)
cv_N2 = 743; %J/(kg K)
R_N2 = cp_N2-cv_N2; %J/(kg K)

%set ICs (temp, pressure,density, velocity, internal energy)
```

```
T_init = 300; %K
p_init = 100000; %N/m^2
rho_init = p_init/(R_N2*T_init); %kg/m^3
u_init = 0; %m/s
e_init = cv_N2*T_init; %J/kg

p_amb = 0; %pressure in tube before shot

%% Simulation Parameters
dx=0.001; % m
t_final = 2e-4; %s

CFL = .1; %Courant number
max_x_pos = 1; %used to define Data matrix
K2 = .25; %2nd order viscosity parameter
K4 = 0.05; %4th order viscosity parameter

dx_firing_pin = 0.02;%setback of firing pin

record_int = 100; %how frequently simulation data is saved

%% Propellant Properties
n_pr = 0.2126; %exponent of burn rate law
beta = (2.014/100)*(1/10^6)^n_pr; %beta of burn rate law
rho_pr = 1910; %kg/m^3 density

%% Initial geometry
proj_length = .0513; %projectile length(m)
x_init = 2.0288-proj_length   ; %initial position of projectile (m)
x_pos = x_init; %current position of back of projectile (m)

mass_proj = 0.2; %projectil mass (kg)
```

```
proj_x = (0+dx/2):dx:(proj_length-dx/2); %projectile cell center positions (m)

N_steps_proj = max(size(proj_x)); %number of cell centers in proj
N_steps_tube = floor(x_pos/dx); %number of cell centers in launch tube
d1 = proj_length-proj_x(end); %upstream section of dx
d2 = (dx/2)+(x_init-N_steps_tube.*dx); %downstream section of dx
dx_IF = d1+d2;% dx at interface

tube_x = (proj_x(end)+dx_IF):dx:(proj_length+x_pos); %tube cell center pos (m)
x = [proj_x tube_x]; % cell center positions (m)

v_proj = 0; %Initial projectile velocity (m/s)
accel = 0;%Initial projectile acceleration (m/s^2)

N_steps = max(size(x)); %number of steps

[r_gc,r_wall,Vol_pr,i_tube] = geometry_full(x); %output radius of gas ...
   column, radius of wall, vol of gunpowder
A_proj = pi*r_gc(1:N_steps_proj).^2; %area vector
A_wall = pi*r_wall(1:N_steps_proj).^2; %area with no propellant
Area_tube = pi*r_gc(N_steps_proj+1).^2;

A_tube = pi*r_gc(N_steps_proj+1:end).^2;%create area matrix

mass_init_pr = Vol_pr*rho_pr; %initial propellant mass
tic; %timing for waitbar start

%% Initialize Data Structures
t_steps = 0; %initialize time step counter

%U of projectile domain
U_proj = [rho_init;rho_init*u_init; rho_init*(e_init+u_init^2/2)]*A_proj;
F_proj = [rho_init*u_init;(rho_init*u_init^2+p_init);...
```

```
rho_init*u_init*(e_init+u_init^2/2+p_init/rho_init)]*A_proj;

%U of launch tube domain
U_tube = [rho_init;rho_init*u_init; rho_init*(e_init+u_init^2/2)]*A_tube;
F_tube = [rho_init*u_init;(rho_init*u_init^2+p_init);...
rho_init*u_init*(e_init+u_init^2/2+p_init/rho_init)]*A_tube;

%Specific heat vectors
CP = cp_N2*ones(1,N_steps);
CV = cv_N2*ones(1,N_steps);
CP_prod = zeros(1,N_steps);
CV_prod = zeros(1,N_steps);
CP_new = ones(1,N_steps);
CV_new = ones(1,N_steps);

%Simulation data matrix
max_cells = ceil(max_x_pos/dx);
Data = zeros(10,max_cells,1);
Motion_Data = zeros(1,4);

%time
Time = [0];
t = 0;

%create waitbar
f = waitbar(0,'Running...');

%% Time-stepping

[T_f, rho_f, CP_f, CV_f, R_f, gamma_f, a_f] = flameTemp(p_init);
%Nominal values:
%T_f = 3.96918e3; rho_f = 6.8715; CP_f = 3.4102e3; CV_f = 2.982769176943934e3;
% R_f = 2.246544123209943e+02; gamma_f = 1.1433; a_f = 1.0097e+03;
```

```
while t<t_final
    %% Find U_bar

    %create derivative matrices
    dU_proj = zeros(3,N_steps_proj);
    dU_tube = zeros(3,N_steps_tube);
    dU_bar_proj = zeros(3,N_steps_proj);
    dU_bar_tube = zeros(3,N_steps_tube);

    %get flow vars
    [rho_proj,p_proj,u_proj,T_proj,e_proj,F_proj] = UtoFlowVars(U_proj,...
    A_proj,CP(1:N_steps_proj),CV(1:N_steps_proj));
    [rho_tube,p_tube,u_tube,T_tube,e_tube,F_tube] = UtoFlowVars(U_tube,...
    A_tube,CP(N_steps_proj+1:end),CV(N_steps_proj+1:end));

    %create area matrix
    A = [A_proj A_tube];
    A_matrix = [0; 1; 0]*A;

    %find sound speeds
    a_proj = real(sqrt((CP(1:N_steps_proj)./CV(1:N_steps_proj)).*...
    (CP(1:N_steps_proj)-CV(1:N_steps_proj)).*T_proj));
    a_tube = real(sqrt((CP(N_steps_proj+1:end)./CV(N_steps_proj+1:end)).*...
    (CP(N_steps_proj+1:end)-CV(N_steps_proj+1:end)).*T_tube));

    %calculate timestep
    dt_mat = [CFL*(dx./(a_proj+abs(u_proj))) CFL*(dx./(a_tube+abs(u_tube)))];
    dt = min(dt_mat);

    %calculate source vector
    r_b = beta.*(p_proj).^n_pr;
    J = zeros(3,N_steps_proj);
```

```
for i = 1:N_steps_proj
    if A_proj(i)≥A_wall(i)
        r_b(i)=0; %set burn rate to zero if no propellant
    else %calculate burn rate, source vector
        P_b = 2*sqrt(A_proj(i).*pi);
        h_f = CP_f*T_f;
        CP_prod(i) = CP_f;
        CV_prod(i) = CP_f;
        J(:,i) = [P_b*r_b(i)*rho_pr; 0; P_b*r_b(i)*rho_pr*h_f];
    end
end

%interface values
u_proj_IF = u_tube(1)+v_proj;
F_proj_IF = [rho_tube(1)*u_proj_IF;(rho_tube(1)*u_proj_IF^2+p_tube(1));...
rho_tube(1)*u_proj_IF*(CV(N_steps_proj+1).*T_tube(1)+u_proj_IF^2/2+...
p_tube(1)/rho_tube(1))].*A(N_steps_proj+1);
u_tube_IF = u_proj(end)-v_proj;
F_tube_IF = ...
   [rho_proj(end)*u_tube_IF;(rho_proj(end)*u_tube_IF^2+p_proj(end));...
rho_proj(end)*u_tube_IF*(CV(N_steps_proj).*T_proj(end)+...
u_tube_IF^2/2+p_proj(end)/rho_proj(end))].*A(N_steps_proj);

%Forward-Backward
if mod(t_steps,2) == 0
    %Find dU including BCs
    p_R = 2*p_tube(end)-p_tube(end-1);  %end wall pressure
    F_R = [0; p_R.*A_tube(end); 0];
    dU_proj(:,1:end-1) = ...
       J(:,1:end-1)-(F_proj(:,2:end)-F_proj(:,1:end-1))./dx+...
    p_proj(1:end-1).*(A_matrix(:,2:N_steps_proj)-A_matrix(:,1:N_steps_proj-1))./dx;
    dU_proj(:,end) = ...
       J(:,end)-(F_proj_IF-F_proj(:,end))/dx_IF+p_proj(end).*...
```

```
    (A_matrix(:,N_steps_proj+1)-A_matrix(:,N_steps_proj))./dx_IF;
    dU_tube(:,1:end-1) = ...
       -(F_tube(:,2:end)-F_tube(:,1:end-1))./dx+p_tube(1:end-1).*...
    (A_matrix(:,N_steps_proj+2:end)-A_matrix(:,N_steps_proj+1:end-1))./dx;
    dU_tube(:,end) = -(F_R-F_tube(:,end))./dx...
    +p_tube(end).*(A_matrix(:,end)-A_matrix(:,end-1))./dx;
else %Backward-Forward
    p_L = 2*p_proj(1)-p_proj(2); %end wall pressure
    F_L = [0; p_L.*A_proj(1); 0];
    dU_proj(:,2:end) = ...
       J(:,2:end)-(F_proj(:,2:end)-F_proj(:,1:end-1))./dx+...
    p_proj(2:end).*(A_matrix(:,2:N_steps_proj)-A_matrix(:,1:N_steps_proj-1))./dx;
    dU_proj(:,1) = ...
       J(:,1)-(F_proj(:,1)-F_L)./dx+p_proj(1).*(A_matrix(:,2)-A_matrix(:,1))./dx;
    dU_tube(:,1) = ...
       -(F_tube_IF-F_tube(:,1))./dx_IF+p_tube(1).*(A_matrix(N_steps_proj)-...
    A_matrix(N_steps_proj+1))./dx_IF;
    dU_tube(:,2:end) = ...
       -(F_tube(:,2:end)-F_tube(:,1:end-1))./dx+p_tube(2:end).*...
    (A_matrix(:,N_steps_proj+2:end)-A_matrix(:,N_steps_proj+1:end-1))./dx;
end

dArea = 2*sqrt(A_proj.*pi).*r_b;

%Find Ubar
U_bar_proj = U_proj + dU_proj.*dt;
U_bar_tube = U_tube + dU_tube.*dt;
%Find Abar
A_bar_proj = A_proj + dArea.*dt;
A_bar_tube = A_tube;

U_bar = [U_bar_proj U_bar_tube];
A_bar = [A_bar_proj A_bar_tube];
```

```
%% Calculate second order artificial diffusion and 4th order hyperdiff
%Initialize matrices
nu = zeros(1,N_steps);
d_R1 = zeros(3,N_steps);
d_L1 = zeros(3,N_steps);
d_R = zeros(3,N_steps);
d_L = zeros(3,N_steps);

%calculate p and nu matrices
p = [p_proj p_tube];
nu(2:end-1)=abs(p(3:end)-2*p(2:end-1)+p(1:end-2))./(abs(p(3:end))...
+abs(2*p(2:end-1))+abs(p(1:end-2)));

%find epsilon values
E2_R = K2.*[max(nu(2:end),nu(1:end-1)) 0];
E4_R = max(0,(K4-E2_R));

%assign relative interface velocities
u_proj_IF2 = u_tube(2)+v_proj;
u_tube_IF2 = u_proj(end-1)-v_proj;

%create interface matrices
U_R_proj = [rho_tube(1); rho_tube(1).*u_proj_IF; ...
    rho_tube(1).*(CV(N_steps_proj+1).*T_tube(1)+u_proj_IF^2/2)]*A(N_steps_proj+1);
U_L_tube = [rho_proj(N_steps_proj); rho_proj(N_steps_proj).*u_proj_IF; ...
    rho_proj(N_steps_proj).*(CV(N_steps_proj).*...
T_proj(N_steps_proj)+u_proj_IF^2/2)]*A(N_steps_proj);
U_R_proj2 = [rho_tube(2); rho_tube(2).*u_proj_IF2; ...
    rho_tube(2).*(CV(N_steps_proj+2).*T_tube(2)+u_proj_IF2^2/2)]*A(N_steps_proj+2);
U_L_tube2 = ...
    [rho_proj(N_steps_proj-1);rho_proj(N_steps_proj-1).*u_proj_IF2;...
rho_proj(N_steps_proj-1).*(CV(N_steps_proj-1).*T_proj(N_steps_proj-1)...
```

```
 +u_proj_IF2^2/2)]*A(N_steps_proj-1);

%find d_L and d_R
d_R1(:,1:N_steps_proj-1) ...
   =E2_R(1:N_steps_proj-1).*(U_proj(:,2:N_steps_proj)-U_proj(:,1:N_steps_proj-1));
d_R1(:,N_steps_proj) = ...
   E2_R(N_steps_proj).*(U_R_proj-U_proj(:,N_steps_proj));
d_R1(:,N_steps_proj+1:end-1) = ...
   E2_R(N_steps_proj+1:end-1).*(U_tube(:,2:end)-U_tube(:,1:end-1));

d_R(:,2:N_steps_proj-2) = ...
   d_R1(:,2:N_steps_proj-2)-E4_R(2:N_steps_proj-2).*(U_proj(:,4:N_steps_proj)-...
3*U_proj(:,3:N_steps_proj-1)+3*U_proj(:,2:N_steps_proj-2)-U_proj(:,1:N_steps_proj-3));
d_R(:,N_steps_proj-1) = ...
   d_R1(:,N_steps_proj-1)-E4_R(N_steps_proj-1).*(U_R_proj-...
3*U_proj(:,N_steps_proj)+3*U_proj(:,N_steps_proj-1)-U_proj(:,N_steps_proj-2));
d_R(:,N_steps_proj) = ...
   d_R1(:,N_steps_proj)-E4_R(N_steps_proj).*(U_R_proj2...
-3*U_R_proj+3*U_proj(:,N_steps_proj)-U_proj(:,N_steps_proj-1));
d_R(:,N_steps_proj+1) = d_R1(:,N_steps_proj+1)...
-E4_R(N_steps_proj+1).*(U_tube(:,3)-3.*U_tube(:,2)+3.*U_tube(:,1)-U_L_tube);
d_R(:,N_steps_proj+2:end-2) = ...
   d_R1(:,N_steps_proj+2:end-2)-E4_R(N_steps_proj+2:end-2).*(U_tube(:,4:end)...
-3*U_tube(:,3:end-1)+3*U_tube(:,2:end-2)-U_tube(:,1:end-3));


E2_L = K2.*[0 max(nu(1:end-1),nu(2:end))];
E4_L = max(0,K4-E2_L);

d_L1(:,2:N_steps_proj) ...
   =E2_L(2:N_steps_proj).*(U_proj(:,2:N_steps_proj)-U_proj(:,1:N_steps_proj-1));
d_L1(:,N_steps_proj+1) = E2_L(N_steps_proj+1).*(U_tube(:,1)-U_L_tube);
d_L1(:,N_steps_proj+2:end) = ...
```

```
    E2_L(N_steps_proj+2:end).*(U_tube(:,2:end)-U_tube(:,1:end-1));

d_L(:,3:N_steps_proj-1) = d_L1(:,3:N_steps_proj-1)-...
E4_L(3:N_steps_proj-1).*(U_proj(:,4:N_steps_proj) ...
    -3*U_proj(:,3:N_steps_proj-1)...
+3*U_proj(:,2:N_steps_proj-2)-U_proj(:,1:N_steps_proj-3));
d_L(:,N_steps_proj) = ...
    d_L1(:,N_steps_proj)-E4_L(N_steps_proj).*(U_R_proj...
-3*U_proj(:,N_steps_proj)+3*U_proj(:,N_steps_proj-1)-U_proj(:,N_steps_proj-2));
d_L(:,N_steps_proj+1) = ...
    d_L1(:,N_steps_proj+1)-E4_L(N_steps_proj+1).*(U_tube(:,2)...
-3*U_tube(:,1)+3*U_L_tube-U_L_tube2);
d_L(:,N_steps_proj+2) = ...
    d_L1(:,N_steps_proj+2)-E4_L(N_steps_proj+2).*(U_tube(:,3)...
-3*U_tube(:,2)+3.*U_tube(:,1)-U_L_tube);
d_L(:,N_steps_proj+3:end-1) = ...
    d_L1(:,N_steps_proj+3:end-1)-E4_L(N_steps_proj+3:end-1).*(U_tube(:,4:end)...
-3*U_tube(:,3:end-1)+3*U_tube(:,2:end-2)-U_tube(:,1:end-3));

D = d_R-d_L;

%% Find Corrected Unew
%find bar vals
%Repeat process above with bar values
[rho_bar_proj,p_bar_proj,u_bar_proj,T_bar_proj,e_bar_proj,F_bar_proj] ...
    = ...
    UtoFlowVars(U_bar_proj,A_bar_proj,CP(1:N_steps_proj),CV(1:N_steps_proj));
[rho_bar_tube,p_bar_tube,u_bar_tube,T_bar_tube,e_bar_tube,F_bar_tube] ...
    = ...
    UtoFlowVars(U_bar_tube,A_bar_tube,CP(N_steps_proj+1:end),CV(N_steps_proj+1:end));

A_bar_matrix = [0; 1; 0]*A_bar;
```

```
%calculate J_bar
r_b_bar = beta.*(p_bar_proj).^n_pr;
J_bar = zeros(3,N_steps_proj);
for i = 1:N_steps_proj
    if r_b(i)==0
        r_b_bar(i)=0;
    else
        P_b = 2*sqrt(A_bar(i).*pi);
        h_f = CP_f*T_f;
        CP_prod(i) = (CP_prod(i)+CP_f)/2;
        CV_prod(i) = (CV_prod(i)+CV_f)/2;
        J_bar(:,i) = [P_b*r_b_bar(i)*rho_pr; 0; ...
           P_b*r_b_bar(i)*rho_pr*h_f];

    end
end

%interface vals
u_bar_proj_IF = u_bar_tube(1)+v_proj;
F_bar_proj_IF = ...
   [rho_bar_tube(1)*u_bar_proj_IF;(rho_bar_tube(1)*u_bar_proj_IF^2+p_bar_tube(1));...
rho_bar_tube(1)*u_bar_proj_IF*(CV(N_steps_proj+1).*T_bar_tube(1)+...
u_bar_proj_IF^2/2+p_bar_tube(1)/rho_bar_tube(1))].*A_bar(N_steps_proj+1);
u_bar_tube_IF = u_bar_proj(end)-v_proj;
F_bar_tube_IF = ...
   [rho_bar_proj(end)*u_bar_tube_IF;(rho_bar_proj(end)*u_bar_tube_IF^2+...
p_bar_proj(end));rho_bar_proj(end)*u_bar_tube_IF*(CV(N_steps_proj).*T_bar_proj(end)...
+u_bar_tube_IF^2/2+p_bar_proj(end)/rho_bar_proj(end))].*A_bar(N_steps_proj);


if mod(t_steps,2) == 0
    p_R = 2*p_bar_tube(end)-p_bar_tube(end-1);
    F_bar_R = [0; p_R.*A_bar_tube(end); 0];
```

```
    dU_bar_proj(:,1:end-1) = ...
       J_bar(:,1:end-1)-(F_bar_proj(:,2:end)-F_bar_proj(:,1:end-1))./dx...
    +p_bar_proj(1:end-1).*(A_bar_matrix(:,2:N_steps_proj)...
    -A_bar_matrix(:,1:N_steps_proj-1))./dx;
    dU_bar_proj(:,end) = ...
       J_bar(:,end)-(F_bar_proj_IF-F_bar_proj(:,end))/dx_IF...
    +p_bar_proj(end).*(A_bar_matrix(:,N_steps_proj+1)...
    -A_bar_matrix(:,N_steps_proj))./dx_IF;
    dU_bar_tube(:,1:end-1) = ...
       -(F_bar_tube(:,2:end)-F_bar_tube(:,1:end-1))./dx+...
    p_bar_tube(1:end-1).*(A_bar_matrix(:,N_steps_proj+2:end)...
    -A_bar_matrix(:,N_steps_proj+1:end-1))./dx;
    dU_bar_tube(:,end) = -(F_bar_R-F_bar_tube(:,end))./dx...
    +p_bar_tube(end).*(A_bar_matrix(:,end)-A_bar_matrix(:,end-1))./dx;
else
    p_L = 2*p_bar_proj(1)-p_bar_proj(2);
    F_bar_L = [0; p_L.*A_bar_proj(1); 0];
    dU_bar_proj(:,2:end) = J_bar(:,2:end)-(F_bar_proj(:,2:end)...
    -F_bar_proj(:,1:end-1))./dx+p_bar_proj(2:end).*...
    (A_bar_matrix(:,2:N_steps_proj)-A_bar_matrix(:,1:N_steps_proj-1))./dx;
    dU_bar_proj(:,1) = J_bar(:,1)-(F_bar_proj(:,1)-F_bar_L)./dx...
    +p_bar_proj(1).*(A_bar_matrix(:,2)-A_bar_matrix(:,1))./dx;
    dU_bar_tube(:,1) = -(F_bar_tube_IF-F_bar_tube(:,1))./dx_IF...
    +p_bar_tube(1).*(A_bar_matrix(N_steps_proj)...
    -A_bar_matrix(N_steps_proj+1))./dx_IF;
    dU_bar_tube(:,2:end) = ...
       -(F_bar_tube(:,2:end)-F_bar_tube(:,1:end-1))./dx...
    +p_bar_tube(2:end).*(A_bar_matrix(:,N_steps_proj+2:end)-...
    A_bar_matrix(:,N_steps_proj+1:end-1))./dx;
end

dArea_bar = 2*sqrt(A_bar_proj.*pi).*r_b_bar;
dArea_av = 0.5*(dArea+dArea_bar);
```

```
%find average derivatives
dU_av_proj = 0.5*(dU_proj+dU_bar_proj);
dU_av_tube = 0.5*(dU_tube+dU_bar_tube);

%iterate
U_proj_new = U_proj+dt*dU_av_proj+D(:,1:N_steps_proj);
U_tube_new = U_tube+dt*dU_av_tube+D(:,N_steps_proj+1:end);

A_proj_new = A_proj+dt*dArea_av;

%change to lab reference
u_lab = [(u_proj-v_proj) u_tube];
T_lab = [T_proj T_tube];
p_lab = [p_proj p_tube];
rho_lab = [rho_proj rho_tube];
Mach = u_lab./sqrt((CP./CV).*(CP-CV).*T_lab);

%save data
Motion_Data(t_steps+1,:)=[t x_pos v_proj accel];

%increment time
t=t+dt;
Time(end+1)=t;
t_steps = t_steps+1;

%% Calculate Force
%from pressure
Fp = (p_lab(i_tube-1)-p_amb).*A_proj(i_tube-1);
%from mdot
F_mdot = rho_proj(i_tube-1).*u_proj(i_tube-1).^2.*A_proj(i_tube-1);
%total thrust
F_tot = Fp+F_mdot;
```

```
%Record Vars
  x_fixed = x-(max(x)+dx/2)+max_x_pos;
  if mod(t_steps,record_int)==0
      data_i = data_i+1;
      Data(:,1:N_steps,data_i) = [x_fixed;rho_lab; p_lab; u_lab; T_lab; ...
          Mach; A; ...
          Fp*ones(1,N_steps);F_mdot*ones(1,N_steps);F_tot*ones(1,N_steps)];
      Time(end+1)=t;
  end

  %save vars
  U_proj = U_proj_new;
  U_tube = U_tube_new;
  A_proj = A_proj_new;

  %waitbar update
  elapsed_time = toc;
  time_rem = round(((t_final-t)/t_final)*(elapsed_time/(t/t_final))/60);

  waitbar(t/t_final,f,sprintf('%12.3f%%, %.f min ...
     remaining',(t/t_final).*100,time_rem))
  pause(0.000001)

  %% Gas constants

  u_local = [u_proj u_tube];
  for i = 1:N_steps
      dm_L = 0;
      dm_R = 0;
      %include added mass from burning propellant
      if N_steps≤max(size(r_b)) && r_b(i)>0
          rb = (r_b(i)+r_b_bar(i))/2;
```

```
    P_b = 2*sqrt(A_bar(i).*pi);
    dm_pr = P_b*r_b_bar(i)*rho_pr*dx*dt;
else
    dm_pr = 0;
end
%calculate velocities and specific heats on each side
if i == 1
    u_L = 0;
    u_R = (u_local(i)+u_local(i+1))/2;
    CP_L = 0; CP_R = CP(i+1);
    CV_L = 0; CV_R = CV(i+1);
elseif i ==N_steps
    u_L = (u_local(i)+u_local(i-1))/2;
    u_R = 0;
    CP_R = 0; CP_L = CP(i-1);
    CV_R = 0; CV_L = CV(i-1);
elseif i == N_steps_proj
    u_L = (u_local(i)+u_local(i-1))/2;
    u_R = (u_local(i)+u_bar_proj_IF)/2;
    CP_L = CP(i-1);
    CV_L = CV(i-1);
    CP_R = CP(i+1);
    CV_R = CV(i+1);
elseif i == N_steps_proj+1
    u_L = (u_local(i)+u_local(i-1))/2;
    u_R = (u_local(i)+u_proj_IF)/2;
    CP_L = CP(i-1);
    CV_L = CV(i-1);
    CP_R = CP(i+1);
    CV_R = CV(i+1);
else
    u_L = (u_local(i)+u_tube_IF)/2;
    u_R = (u_local(i)+u_local(i+1))/2;
```

```
        CP_L = CP(i-1);
        CV_L = CV(i-1);
        CP_R = CP(i+1);
        CV_R = CV(i+1);
    end
    %find mass fluxes from cells on either side
    if u_L ≠ 0
        dm_L = ((rho_lab(i)+rho_lab(i-1))/2)*((A(i)+A(i-1))/2)*u_L*dt;
    end
    if u_R ≠ 0
        dm_R = -((rho_lab(i)+rho_lab(i+1))/2)*((A(i)+A(i+1))/2)*u_R*dt;
    end
    %find new CV and CP
    m_cell = rho_lab(i).*A(i).*dx;
    CP_new(i) = (m_cell.*CP(i)+dm_L.*CP_L+dm_R.*CP_R...
    +dm_pr.*CP_prod(i))/(m_cell+dm_L+dm_R+dm_pr);
    CV_new(i) = (m_cell.*CV(i)+dm_L.*CV_L+dm_R.*CV_R...
    +dm_pr.*CV_prod(i))/(m_cell+dm_L+dm_R+dm_pr);
end

%smooth CPs to elimnate discontinuities
CP = smoothdata(CP_new,'gaussian',2);
CV = smoothdata(CV_new,'gaussian',2);

%% Kinematics
accel = F_tot/mass_proj; %calculate acceleration (m/s^2)
v_proj_new = v_proj +accel.*dt; %new velocity (m/s)
x_pos_new = x_pos +0.5*(v_proj_new+v_proj)*dt; %new position (m)

v_proj = v_proj_new; %reassign
x_pos = x_pos_new; %reassign

if N_steps_tube<floor(x_pos/dx)%remesh (add cells if dx_IF large enough)
```

```
    N_steps_tube = floor(x_pos/dx); %number of cell centers in launch tube
    d1 = proj_length-proj_x(end); %upstream section of dx
    d2 = (dx/2)+(x_pos-N_steps_tube.*dx); %downstream section of dx
    dx_IF = d1+d2;% dx at interface

    tube_x = (proj_x(end)+dx_IF):dx:(proj_length+x_pos); %tube cell ...
       center pos (m)
    x = [proj_x tube_x]; % cell center positions (m)
    N_steps = max(size(x));

    %reassign to new U vector
    [rho_end,p_end,u_end,T_end,e_end,F_end] = ...
       UtoFlowVars(U_proj(:,end),A_proj(end),CP(N_steps_proj),CV(N_steps_proj));
    u_end_adj= u_end-v_proj;
    Uendproj = [rho_end*A_proj(end);rho_end*u_end_adj*A_proj(end);...
    rho_end*(e_end+u_end_adj^2/2)*A_proj(end)];
    U_int = Uendproj+(dx_IF/(dx_IF+dx))*(U_tube(:,1)-Uendproj);

    U_tube = [U_int U_tube];
    A_tube = [Area_tube A_tube];

    %linear interp gas properties for new cell
    CP_int = ...
       CP(N_steps_proj)+(dx_IF/(dx_IF+dx))*(CP(N_steps_proj+1)-CP(N_steps_proj));
    CV_int = ...
       CV(N_steps_proj)+(dx_IF/(dx_IF+dx))*(CV(N_steps_proj+1)-CV(N_steps_proj));

    CP = [CP(1:N_steps_proj) CP_int CP(N_steps_proj+1:end)];
    CV = [CV(1:N_steps_proj) CV_int CV(N_steps_proj+1:end)];
end
```

```
end
close(f)

%% Plot
figure(1)
for n = 1:10:t_steps
    subplot(5,1,1),
    plot(Data(1,:,t_steps),Data(3,:,n),'.'),axis([0 x_init -Inf ...
        Inf]),ylabel('Pressure (Pa)')
    subplot(5,1,2),
    plot(Data(1,:,t_steps),Data(4,:,n),'.'),axis([0 x_init -Inf ...
        Inf]),ylabel('Velocity (m/s)')
    subplot(5,1,3),
    plot(Data(1,:,t_steps),Data(6,:,n),'.'),axis([0 x_init -Inf ...
        Inf]),ylabel('Mach')
    subplot(5,1,4),
    plot(Data(1,:,t_steps),Data(5,:,n),'.'),axis([0 x_init 0 ...
        Inf]),ylabel('Temp (K)')
    subplot(5,1,5),
    plot(Data(1,:,t_steps),sqrt(Data(7,:,n)./pi)),axis([0 x_init 0 ...
        Inf]),ylabel('Temp (K)'),xlabel('x_loc (m)')
    drawnow
end
yy = zeros(1,t_steps);
for i = 1:t_steps
    yy(i) = Data(end,1,i);
end
figure(2)
subplot(4,1,1),plot(Time(1:end-1),yy),ylabel('Thrust (N)')
subplot(4,1,2),plot(Motion_Data(:,1),Motion_Data(:,2)),ylabel('position (m)')
subplot(4,1,3),plot(Motion_Data(:,1),Motion_Data(:,3)),ylabel('velocity ...
    (m/s)')
subplot(4,1,4),plot(Motion_Data(:,1),Motion_Data(:,4)),xlabel('time (s)'), ...
```

```
ylabel('accel (m/s^2)')
```

C.2 MATLAB Code - `geometry.m`

```
%geometry.m - outputs the geometry profile of the computational domain
%
% Syntax:  [r_gc,r_w,V_tot,theta] = geometry(x)
%
% Inputs:
%    x - input matrix of x locations
%
% Outputs:
%    r_gc - matrix of the radius of gas column at each point
%    r_w - matrix of the wall at each point (difference from r_gc is ...
   propellant)
%    V_tot - total volume of propellant
%    theta - angle at each point
%
% Author: Clayton Davis
%
% email: daviscw@uw.edu
%
% Jan 2019; Last revision: 8-Feb-2019
function [r_gc,r_w,V_tot,theta] = geometry(x)
%define radii and requisite lengths
r_inner = 0.005;
r_outer = 0.007;
r_throat = 0.002;
r_tube = 0.019;
l_a = 0.03;
l_b = 0.015;
l_c = 0.022;

%set vars for cubic splines
```

```
x1 = l_a;
y1 = r_outer;
x2 = l_a+l_b;
y2 = r_throat;
x3 = l_a+l_b+l_c;
y3 = r_tube;
%create matrices for lines of best fit
A1 = [x1.^3 x1.^2 x1 1; x2.^3 x2.^2 x2 1; 3*x1.^2 2*x1 1 0; 3*x2.^2 2*x2 1 0];
A2 = [x2.^3 x2.^2 x2 1; x3.^3 x3.^2 x3 1; 3*x2.^2 2*x2 1 0; 3*x3.^2 2*x3 1 0];

Y1 = [y1; y2; 0; 0]; Y2 = [y2; y3; 0; 0];

C1 = inv(A1)*Y1;
C2 = inv(A2)*Y2;

%find end point of propellant
syms xsym
x0 = vpasolve(r_inner == ...
    C1(1)*xsym^3+C1(2)*xsym^2+C1(3)*xsym+C1(4),xsym,(x1+x2)/2);
x0= double(x0(2));

%find total volume
fun = @(xsym) pi*(C1(1)*xsym.^3+C1(2)*xsym.^2+C1(3)*xsym+C1(4)).^2;
V_int = integral(fun,l_a,x0);
V_tot = pi*r_outer.^2*l_a+V_int- pi*r_inner.^2*x0;

%create empty matrices
r_w = zeros(1,max(size(x)));
r_gc = zeros(1,max(size(x)));
theta = zeros(1,max(size(x)));

%loop through output matrices assigning vals
for i = 1:max(size(x))
```

```
    if x(i)<0
        r_gc(i) = 0;
        r_w(i) = 0;
        theta(i) = 0;
    elseif x(i)<l_a
        r_gc(i)=r_inner;
        r_w(i) = r_outer;
        theta(i) = 0;
    elseif x(i)<x0
        r_gc(i) = r_inner;
        r_w(i) =  C1(1).*x(i)^3+C1(2).*x(i)^2+C1(3).*x(i)+C1(4);
        theta(i) = atan(3.*C1(1).*x(i).^2+2.*C1(2).*x(i)+C1(3));
    elseif x(i)<l_a+l_b
        r_gc(i) = C1(1).*x(i)^3+C1(2).*x(i)^2+C1(3).*x(i)+C1(4);
        r_w(i) =  C1(1).*x(i)^3+C1(2).*x(i)^2+C1(3).*x(i)+C1(4);
        theta(i) = atan(3.*C1(1).*x(i).^2+2.*C1(2).*x(i)+C1(3));
    elseif x(i)<l_a+l_b+l_c
        r_gc(i) = C2(1).*x(i)^3+C2(2).*x(i)^2+C2(3).*x(i)+C2(4);
        r_w(i) = C2(1).*x(i)^3+C2(2).*x(i)^2+C2(3).*x(i)+C2(4);
        theta(i) = atan(3.*C2(1).*x(i).^2+2.*C2(2).*x(i)+C2(3));
    else
        r_w(i) = r_tube;
        r_gc(i) = r_tube;
        theta(i) = 0;
    end
end
end
```

C.3 MATLAB Code - `flameTemp.m`

```
%-------------------------------------------------------------
% FUNCTION flameTemp.m
% This function runs CEA on blackpowder mixture at input pressure
% to find adiabatic flame temp and gas props of combustion products.
% INPUTS
% P     - combustion pressure (N/m^2)
%
% OUTPUTS
% T     - flame temperature (K)
% RHO   - product density (kg/m^3)
% Cp    - product Cp J/(kg K)
% Cv    - product Cv J/(kg K)
% R     - product R J/(kg K)
% gamma - ratio of specific heats (-)
% a     - sonic velocity (m/s)
%
% FORTRAN code required: FCEA2
%
% Author: Clayton Davis
%
% email: daviscw@uw.edu
%
% Jan 2019; Last revision: 8-Feb-2019
%-------------------------------------------------------------

function [T, RHO, Cp, Cv, R, gamma, a] = flameTemp(P)
P = P/100000;%convert N/m^2 to bar
R_gas = 8314.4598; %J/(K mol) gas constant

%create input string to CEA
```

```
str = 'blackpowder';
FID_in = fopen([str '.inp'],'w');
fprintf(FID_in,['prob\nhp p,bar=%.2f t,k=3800\n'...
    'react\n'...
    '  fuel=C moles=8 t,k=300\n'...
    '  fuel=S moles=3 t,k=300\n'...
    '  oxid=KNO3 moles=10 t,k=300\n'...
    'output\n'...
    '     siunits\n'...
    '    plot p t rho\n'...
    'end\n' ],P);

fclose(FID_in);

%run fortran code
[status,cmdout]=system(['printf ''' str '\n'' | ...
   /Users/clay/Desktop/RocketTube/FCEA2']);
%parse outputs from file
fileout = fileread([str '.out']);
index1 = strfind(fileout,'T, K');
index2 = strfind(fileout,'RHO, KG/CU M');
index3 = strfind(fileout,'Cp, KJ/(KG)(K)');
index4 = strfind(fileout,'GAMMAs');
index5 = strfind(fileout,'SON VEL,M/SEC');
index6 = strfind(fileout,'M, (1/n)');

%assign values from parsed info
T = str2double(fileout(index1+17:index1+23));
RHO_str = fileout(index2+16:index2+23);
RHO = str2double(RHO_str(1:6))*(10^str2double(RHO_str(7:8)));
Cp = 1000*str2double(fileout(index3+16:index3+23));
gamma = str2double(fileout(index4+16:index4+23));
a = str2double(fileout(index5+16:index5+23));
```

```
M = str2double(fileout(index6+16:index6+22));
Cv = Cp/gamma;
R = R_gas*(1/M);

end
```